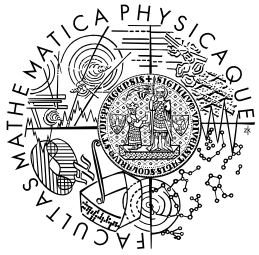

FACULTY
OF MATHEMATICS
AND PHYSICS
Charles University

BACHELOR THESIS

Tomáš Formánek

Source regions of type III solar radio emissions

Department of Surface and Plasma Science

Supervisor of the bachelor thesis: prof. RNDr. Ondřej Santolík, Dr.
Study programme: Physics (B0533A110001)
Study branch: FP (0533RA110001)

Prague 2024

I declare that I carried out this bachelor thesis independently, and only with the cited sources, literature and other professional sources. It has not been used to obtain another or the same degree.

I understand that my work relates to the rights and obligations under the Act No. 121/2000 Sb., the Copyright Act, as amended, in particular the fact that the Charles University has the right to conclude a license agreement on the use of this work as a school work pursuant to Section 60 subsection 1 of the Copyright Act.

In ..... date ....

Author's signature

I would like to thank my supervisor Prof Ondřej Santolík for his patience and thoughtful advice, which he provided throughout my work on this thesis. I must also thank my advisors Dr David Píša and Dr Jan Souček for the many useful insights into the data analysis. The collective knowledge and insightful guidance of my advisors and supervisor proved invaluable in completing this thesis.
My gratitude also extends to Dr Daniel Verscharen for his technical advice with the ALPS software and to Prof Christopher Owen and Dr Georgios Nicolaou for their insights regarding the electron observational data.
And last but not least I want to thank my family for their unwavering support throughout my studies.

I acknowledge the financial support provided by the Support for the Internationalisation of Charles University programme, grant POINT/a/2023-2-062, and by the GAČR grant 22-10775S.

Title: Source regions of type III solar radio emissions

Author: Tomáš Formánek

Department: Department of Surface and Plasma Science

Supervisor: prof. RNDr. Ondřej Santolík, Dr., Department of Surface and Plasma Science

Abstract: Investigating the source regions of solar type III radio emissions, this thesis focuses on understanding the generation and properties of Langmuir waves. Beginning with an introduction to solar wind dynamics and kinetic plasma theory, we lay the theoretical groundwork for numerically solving the hot plasma dispersion relation. Utilizing observational electron velocity distribution data collected by the Solar Orbiter spacecraft, we develop models of the electron velocity distribution function. We explore the stability of the electron distributions using the ALPS dispersion relation solver. We investigate the properties of observed electric waveforms by performing a Hilbert transformation, revealing the presence of multiple wave modes and their frequency distributions. This thesis contributes to our understanding of the mechanisms underlying the generation of type III radio emissions in the solar wind, particularly studying the growth of Langmuir waves.

Keywords: solar wind waves and instabilities in plasmas solar radio emissions

Název: Zdrojové oblasti slunečních radiových emisí typu III

Autor: Tomáš Formánek

Katedra: Katedra fyziky povrchů a plazmatu

Vedoucí bakalářské práce: prof. RNDr. Ondřej Santolík, Dr., Katedra fyziky povrchů a plazmatu

Abstrakt: V této práci se zabýváme výzkumem zdrojových oblastí slunečních rádiových emisí typu III se zaměřením na růst a vlastnosti Langmuirových vln. Počínaje přehledem dynamiky slunečního větru a kinetické teorie plazmatu uvádíme teoretický základ pro numerické řešení disperzní relace v horkém plazmatu. S využitím naměřených částicových dat ze sondy Solar Orbiter vyvíjíme modely rychlostní rozdělovací funkce elektronů. Pomocí numerického řešiče disperzní relace ALPS dále zkoumáme stabilitu rozdělení elektronů. Pomocí Hilbertovy transformace provádíme analýzu vlastností pozorovaných elektrických vln. Odhalujeme přítomnost více vlnových módů a jejich frekvenční rozložení. Tato práce přispívá k pochopení mechanismů, které hrají roli ve vzniku rádiových emisí typu III ve slunečním větru, se zaměřením na růst Langmuirových vln.

Klíčová slova: sluneční vítr vlny a nestability v plazmatu sluneční rádiové emise

Contents

Introduction

The Sun broadcasts its activity throughout the solar system in various ways. Its photosphere, heated to thousands of Kelvin, emits a broad spectrum of electromagnetic radiation providing visible light and radiating heat into the vast solar system. However, beyond the reach of the human eye lies a hidden realm of solar activity. To investigate the dynamic phenomena within the solar wind, which arise from the solar activity, we can use both scientific spacecraft and ground observations to better our understanding of solar dynamics.

Solar radio emissions are often observed by spacecraft and ground based observatories indicating the Sun's activity. These radio emissions are caused by energetic events at the Sun, which occur during brief periods. During such events, an electron beam can be ejected from the Sun. This electron beam travels from the solar corona into the solar wind, propagating along the magnetic field lines.

As the electron beam interacts with the solar wind plasma, kinetic instabilities cause the growth of Langmuir waves, which in turn modifies the properties of the beam. The Langmuir waves, generated locally along the beams path, cannot propagate far due to the process known as Landau damping.

However, we can still detect this process from afar, because the Langmuir waves undergo a mode conversion process. This generates free space mode electromagnetic waves at the local plasma frequency. This electromagnetic wave is called a type III radio emission.

Several questions still remain to be answered regarding the type III radio emissions. In this work we examine the current understanding of type III radio emissions while focusing on the source regions where the electron beam causes the growth of plasma waves. We will also analyze in situ observations performed by the Solar Orbiter spacecraft in the source regions of type III radio emissions. And show how experimental observations compare to our current understanding of type III radio emissions.

In chapter 1 we introduce the solar wind environment and its typical plasma parameters. We delve into the theory of the plasma dispersion relation, deriving an approach to determining the stability of an electron distribution in velocity space. In chapter 2 we provide a theoretical description of the mechanism growing Langmuir waves and the analytical models that can be used to model the system.

In chapter 3 we introduce the scientific instruments onboard the Solar Orbiter spacecraft and the data products they produce.

In chapter 4 we analyze the observational data of type III radio emissions. We focus on determining the stability of an electron velocity distribution in the source region of a type III emission. Our analysis of observational data is continued in chapter 5, where we analyze the Langmuir waves generated by an electron beam using observed electric waveform data.

1. The solar wind environment

1.1 The discovery of the solar wind

The concept of the solar wind was first introduced by Biermann [1951], when he proposed that a radial flow of charged particles could explain the observed direction of the plasma tails of comets. Building on this idea, Parker [1958] then demonstrated that the coronal pressure is high enough for particles to continuously escape from the Sun. The escaping particles of both polarities (mainly electrons and protons, with a small fraction of heavier positive ions) form a quasineutral plasma medium. After an initial acceleration in the solar corona, the expanding plasma flows radially outward at a large speed, which does not depend on the distance from the Sun. These theoretical inferences earned Parker credit for the solar wind's discovery. However, at the time, his pioneering work was not well-received, and the scientific community was skeptical about the solar wind's existence. It was only with the onset of the space age that conclusive evidence became available, confirming Parker's predictions.

By means of in situ spacecraft observations, much has been discovered about the solar wind since. We now know that our solar system is filled with a turbulent solar wind which carries the Sun's magnetic field. Since that was also one of the predictions of Parker [1958] we call the curved magnetic field lines the Parker spiral. Furthermore, research has unveiled the existence of two types of the solar wind: slow and fast. They differ in their source regions and by the observed solar wind parameters (see table 1.1 adopted from Tsurutani et al. [2023]).

Parameter	**Slow Solar Wind**	**Fast Solar Wind**
Drift velocity	$\sim 300 - 400$ km/s	$\sim 750 - 800$ km/s
Electron density	~ 5 cm^{-3}	~ 3 cm^{-3}
Proton Temperature	$\sim 0.5 \times 10^5$ K	$\sim 2.8 \times 10^5$ K
Electron Temperature	$\sim 1.0 \times 10^5$ K	$\sim 1.3 \times 10^5$ K
Magnetic Intensity	~ 5 nT	~ 5 nT

Table 1.1: Typical plasma parameters of the solar wind at 1 AU

1.2 Magnetohydrodynamic description of the solar wind plasma

To describe plasmas such as the solar wind, we can employ two main approaches: the collisionless kinetic approach and the magnetohydrodynamic (MHD) fluid approach.

The MHD approach, pioneered by Hannes Alfvén, describes plasmas as an electrically conducting fluid. This approach can be understood as an extension of fluid dynamics which takes the electromagnetic forces into account. Despite the apparent simplicity, this approach predicts a range of results, such as the

existence of Alfvén waves by [Alfvén, 1942] or the frozen in magnetic field lines in the solar wind (see section 1.3).

Let us first introduce a few concepts which are fundamental to this approach. To describe the plasma, composed of several species of charged particles, we use a phase space distribution function $f(\mathbf{r}, \mathbf{v}, t)$ with units $[f] = s^3/m^{-6}$. Using f we can obtain measurable parameters of the plasma by averaging over the phase space. In other words, we can take the moments of the phase space distribution. The number density distribution of the s-th species can be obtained by integrating over the velocities as

$$n_s(\mathbf{r}, t) = \int_{\mathbb{R}^3} f_s d^3v, \tag{1.1}$$

where f_s is the distribution function for the s-th species. To obtain an intensive scalar variable, we multiply f by the relevant microscopic variable. For example we obtain the mass density of the s-th species ρ_s as

$$\rho_s(\mathbf{r}, t) = \int_{\mathbb{R}^3} m_s f_s d^3v. \tag{1.2}$$

Vector variables, such as the bulk velocity of the s-th species U_s are also obtained by multiplying f:

$$n_s \mathbf{U}_s = \int_{\mathbb{R}^3} \mathbf{v} f_s d^3v, \tag{1.3}$$

and for tensors, such as the pressure tensor $\overleftrightarrow{\mathbf{P}}_s$ we have

$$\overleftrightarrow{\mathbf{P}}_s = \int_{\mathbb{R}^3} m_s(\mathbf{v} - \mathbf{U}_s)(\mathbf{v} - \mathbf{U}_s) f_s d^3v, \tag{1.4}$$

where the components of the pressure tensor describe the average rate at which momentum is being transferred in a certain direction. If this tensor is isotropic, meaning $\overleftrightarrow{\mathbf{P}}_s = p_s \overleftrightarrow{\mathbf{1}}$, we can later (in equation (1.6)) replace $(\nabla \cdot \overleftrightarrow{\mathbf{P}}_s)$ by (∇p_s).

We can now obtain the equations of motion for a single species fluid. We start with the Boltzmann kinetic equation

$$\frac{\partial f}{\partial t} + \mathbf{v} \cdot \nabla f + \frac{\mathbf{F}}{m} \cdot \nabla_v f = \frac{\delta_c f}{\delta t}, \tag{1.5}$$

where $\mathbf{F}$ is a general force acting upon the plasma and the term on the right hand side is an unspecified collision operator. This equation describes the time evolution of the phase space distribution function f. We multiply this equation for the s-th species by momentum $m_s v_s$ and integrate in velocity space. We get

$$\frac{\partial}{\partial t}(m_s n_s \mathbf{U_s}) + m_s n_s (\mathbf{U}_s \cdot \nabla)\mathbf{U}_s + \nabla \cdot \overleftrightarrow{\mathbf{P}}_s - \int_{\mathbb{R}^3} \mathbf{F} f_s d^3v = \pm \frac{\delta_c \mathbf{p}_s}{\delta t}, \tag{1.6}$$

where the right hand side describes the friction between fluids via collisions. For a more detailed derivation see Gurnett and Bhattacharjee [2017]. If we rearrange

the terms, assume an isotropic pressure tensor and plug in the Lorenz force for $\mathbf{F}$, we get the equation of motion for the s-th species:

$$m_s n_s \frac{d\mathbf{U}_s}{dt} = \pm e n_s (\mathbf{E} + \mathbf{U}_s \times \mathbf{B}) - \nabla p_s \pm \frac{\delta_c \mathbf{p}_s}{\delta t}. \tag{1.7}$$

For simplicity, we consider here only two species: positive ions and negative electrons. By adding equation (1.7) for ions and electrons we get the combined equation of motion of the plasma described as a single fluid

$$\rho \frac{d\mathbf{v}}{dt} = \mathbf{j} \times \mathbf{B} - \nabla p, \tag{1.8}$$

where we define the density ρ, velocity $\mathbf{v}$, current density $\mathbf{j}$ and the pressure p as:

$$\rho = n_i m_i + n_e m_e, \tag{1.9}$$

$$\mathbf{v} = \frac{n_i m_i \mathbf{v}_i + n_e m_e \mathbf{v}_e}{n_i m_i + n_e m_e}, \tag{1.10}$$

$$\mathbf{j} = e(n_i v_i - n_e v_e), \tag{1.11}$$

$$p = p_i + p_e. \tag{1.12}$$

$$\tag{1.13}$$

Similarly we obtain the generalized Ohm's law by subtracting renormalized (1.7) or ions and electrons, and after introducing additional approximative simplifications:

$$\mathbf{j} = \sigma(\mathbf{E} + \mathbf{v} \times \mathbf{B}) + \frac{1}{en}[(\nabla p_e) - \mathbf{j} \times \mathbf{B}]. \tag{1.14}$$

Note that in the anisotropic case the conductivity σ and pressure p become tensors. In the MHD approximation the last term in equation (1.14) is often omitted so that the generalized Ohm's law for MHD becomes

$$\mathbf{j} = \sigma(\mathbf{E} + \mathbf{v} \times \mathbf{B}). \tag{1.15}$$

To fully describe the plasma, a complete set of equations is required. For a two component plasma we have 16 independent variables: $\{n_e, n_i, p_e, p_i, \mathbf{v_e}, \mathbf{v_i}, \mathbf{E}, \mathbf{B}\}$ (vectors count as three independent components). Thus, we need more equations to relate these variables. From fluid dynamics we get the continuity equations for the plasma fluid

$$\frac{\partial \rho}{\partial t} + \nabla \cdot (\rho \mathbf{v}) = 0, \tag{1.16}$$

$$\frac{\partial \rho_q}{\partial t} + \nabla \cdot (\mathbf{j}) = 0. \tag{1.17}$$

Thermodynamics provides us with an equation of state for the plasma

$$p = C\rho^{\gamma}, \tag{1.18}$$

which we can use to relate the pressure to the density. And lastly the Maxwell's equations in the MHD approximation are

$$\nabla \cdot \mathbf{E} = 0 \tag{1.19}$$
$$\nabla \cdot \mathbf{B} = 0 \tag{1.20}$$
$$\nabla \times \mathbf{E} = -\frac{\partial \mathbf{B}}{\partial t} \tag{1.21}$$
$$\nabla \times \mathbf{B} = \mu_0 \mathbf{j}. \tag{1.22}$$

In the MHD approximation we omit the charge density term in (1.19) due to quasi-neutrality of the plasma. We also omit the Maxwell's current from Ampere's law (1.22) using the MHD low frequency approximation.

Equations (1.8) and (1.15) through (1.22) now give a complete set. Although there are more than 16 equations, only 16 of them are independent, as described in [Chen, 1984, chapter 3.3.7].

1.3 Solar wind magnetic field

Using the MHD equations derived in the previous section, we can now show that in a highly conductive plasma, magnetic field lines freeze and are carried by the plasma. To describe the changes in the magnetic field, we will derive the induction equation for a plasma.

Applying the curl operator on the generalized Ohm's law in the MHD approximation (1.15), we obtain

$$\nabla \times \mathbf{j} = \sigma(\nabla \times \mathbf{E} + \nabla \times (\mathbf{v} \times \mathbf{B})). \tag{1.23}$$

Applying the Ampere's law in the low frequency MHD approximation (1.22) to the left hand side and the Maxwell-Faraday equation (1.21) to the $(\nabla \times \mathbf{E})$ term:

$$\nabla \times (\nabla \times \mathbf{B}) = \mu_0 \sigma(-\frac{\partial \mathbf{B}}{\partial t} + \nabla \times (\mathbf{v} \times \mathbf{B})). \tag{1.24}$$

After further simplification we get the induction equation

$$\frac{\partial \mathbf{B}}{\partial t} = \nabla \times (\mathbf{v} \times \mathbf{B}) + \frac{1}{\mu_0 \sigma} \nabla^2 \mathbf{B}. \tag{1.25}$$

Now we can investigate the phenomena of frozen magnetic field lines. For a highly conductive plasma we can omit the last term in the induction equation (1.25). Rearranging the terms we get

$$\frac{\partial \mathbf{B}}{\partial t} - \nabla \times (\mathbf{v} \times \mathbf{B}) = 0. \tag{1.26}$$

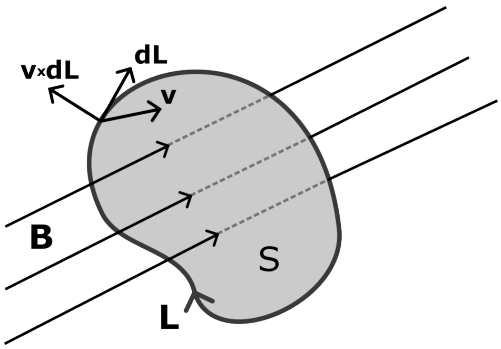

Figure 1.1: Magnetic flux flowing through a closed loop.

Now, using equation (1.26), we can study the change in the magnetic flux Φ going through a closed loop L with the surface S shown in figure 1.1. The change in magnetic flux is given by Faraday's law as

$$\frac{d\Phi}{dt} = \int_S \frac{\partial \mathbf{B}}{\partial t} \cdot \mathbf{dS} + \int_L (\mathbf{B} \times \mathbf{v}) \cdot d\mathbf{L} \tag{1.27}$$

We can rewrite the second term in equation (1.27) using Stokes' theorem as a surface integral, obtaining (1.28) where the term inside the bracket is zero from equation (1.26).

$$\frac{d\Phi}{dt} = \int_S \left(\frac{\partial \mathbf{B}}{\partial t} - \nabla \times (\mathbf{v} \times \mathbf{B}) \right) \cdot d\mathbf{S} = 0 \tag{1.28}$$

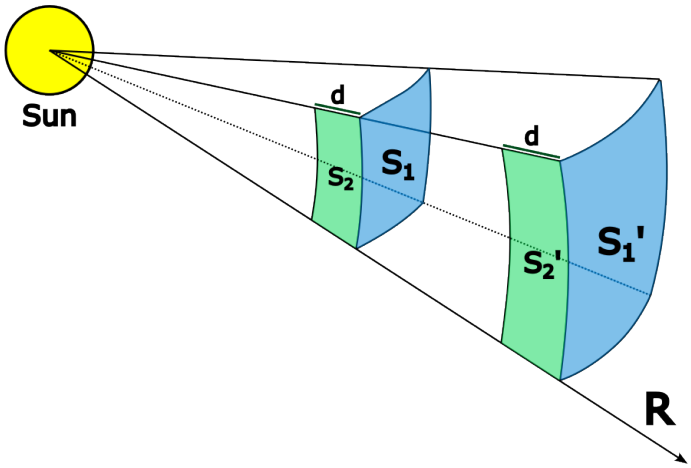

Figure 1.2: A visualization of the time evolution of two surfaces S_1 and S_2 being carried by the expanding Solar wind.

To see how the magnetic field lines are shaped in the Solar wind we now consider two surfaces as shown in figure 1.2. The surfaces S_1 and S_2 are being carried by the Solar wind as it expands away from the Sun.

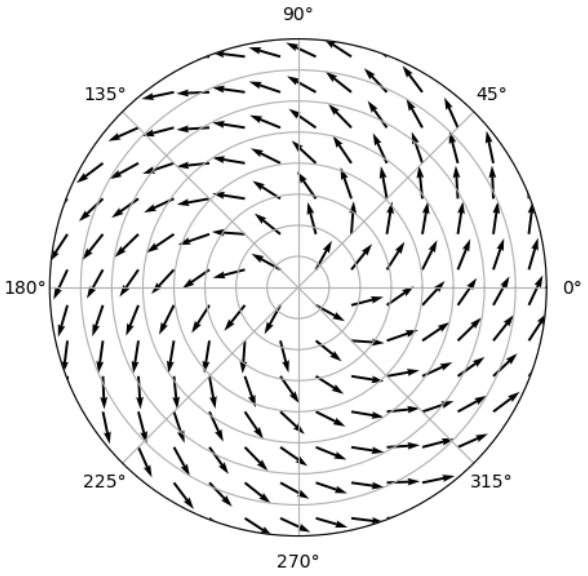

Figure 1.3: Illustration of a vector field depicting the directional dependence of the magnetic field in the solar wind, with the derived radial distance dependencies.

From equation (1.28), we know that the magnetic flux stays constant in the surfaces S_1 and S_2 as they evolve into S_1' and S_2' respectively. Assuming a constant solar wind speed as a function of the radial distance R, the area of the surfaces can be related to R as $S_1 \propto R^2$ and $S_2 \propto R$. And in order for the magnetic flux to stay the same the magnetic field must be related to R as $B_r \propto R^{-2}$ for the radial component and $B_t \propto R^{-1}$ for the tangential component.

Figure 1.3 shows this derived radial distance dependence, visualizing the configuration of magnetic field lines in the equatorial plane of the solar wind. As mentioned earlier, this result was first predicted by Parker [1958].

1.4 Collisionless kinetic approach

The collisionless approach assumes that the plasma interacts primarily via long-range electromagnetic forces and that the collisions play a minor role. For this reason, this approach allows for analyzing single particle motions to study the collective behavior.

1.4.1 Collisionless cold magnetized plasma

In the cold plasma approximation, we assume a plasma that is initially at rest and has no temperature fluctuations ($T_e = T_p = 0$). Using this simple assumption one can obtain powerful results which hold approximately true even for finite temperatures.

To obtain the dispersion relation for waves in cold magnetized plasma, we need to solve the wave equation, which can be easily derived from the Faraday's Law of Induction (1.21)

$$\nabla \times \mathbf{E} = -\frac{\partial \mathbf{B}}{\partial t}$$

and the Ampere's Law with Maxwell's curent

$$\nabla \times \mathbf{B} = \mu_0 \mathbf{j} + \mu_0 \varepsilon_0 \frac{\partial \mathbf{E}}{\partial t} \tag{1.29}$$

To derive the wave equation, we take the curl of Faraday's Law and plug in equation (1.29) for $\mathbf{B}$ on the right hand side. After applying the standard vector identities, we arrive at the wave equation

$$\nabla(\nabla \cdot \mathbf{E}) - \nabla^2 \mathbf{E} + \frac{1}{c^2} \frac{\partial^2 \mathbf{E}}{\partial t^2} + \mu_0 \frac{\partial \mathbf{J}}{\partial t} = 0. \tag{1.30}$$

Now, we can use the relation $\mathbf{j} = \overleftrightarrow{\sigma}\mathbf{E}$ to express the current in terms of $\mathbf{E}$. To solve this equation, we apply the Fourier transform and then use the identity $n = kc/\omega$. After simplifying our result, we get

$$n^2 \hat{\mathbf{k}}\hat{\mathbf{k}} \cdot \mathbf{E} - n^2 \mathbf{E} + \overleftrightarrow{\epsilon}\mathbf{E} \equiv \mathcal{D} \cdot \mathbf{E} = 0. \tag{1.31}$$

To solve equation (1.31), we need to determine the relative permittivity tensor

$$\overleftrightarrow{\epsilon} = \left(\overleftrightarrow{\mathbf{1}} + \frac{i\overleftrightarrow{\sigma}}{\omega \epsilon_0} \right) = (\overleftrightarrow{\mathbf{1}} + \overleftrightarrow{\chi}), \tag{1.32}$$

Which can be done by expressing the current in terms of $\mathbf{E}$:

$$\mathbf{j} = \overleftrightarrow{\sigma}\mathbf{E} = \sum_s n_s q_s \overleftrightarrow{\mu}_s \mathbf{E}. \tag{1.33}$$

To obtain the mobility $\overleftrightarrow{\mu}_s$, we need to investigate the equation of motion for a single particle

$$m_s \frac{d\mathbf{v}_s}{dt} = q_s(\mathbf{E} + \mathbf{v}_s \times \mathbf{B}). \tag{1.34}$$

Performing the Fourier transform in time, we obtain

$$-i\omega \mathbf{v}_s = \frac{q_s}{m_s}(\mathbf{E} + \mathbf{v}_s \times \mathbf{B}). \tag{1.35}$$

From here, we can express the magnetic field amplitude using the cyclotron frequency $\Omega_s = \frac{q_j B}{m_s}$. Setting our coordinate system so that the z-axis is aligned with the magnetic field, equation (1.35) can be rewritten as

$$\mathbf{v}_s = \frac{q_s i}{m_s} \begin{bmatrix} \omega & i\Omega_s & 0 \\ -i\Omega_s & \omega & 0 \\ 0 & 0 & \omega \end{bmatrix}^{-1} \mathbf{E} = \overleftrightarrow{\mu}_s \mathbf{E}. \tag{1.36}$$

Now, we can obtain the cold plasma permittivity and solve the dispersion relation (1.31). This equation is equivalent to finding the roots of the determinant

of $\mathcal{D}$. This can be done explicitly for cold plasma and allows for studying various wave modes, such as the Z-mode, whistler waves or the free space modes. The detailed derivation can be found in [Gurnett and Bhattacharjee, 2017, chapter 4]. And a summary of the results relevant to our analysis of type III radio emissions can be found in section 2.2.

1.4.2 Hot plasma dispersion relation

The Langmuir instability is an electron beam driven instability. The thermal effects of hot plasma play an important role in determining the conditions for instability since it is driven by Landau resonant electrons. For that reason, the cold plasma approach cannot be used to study the growth corresponding to Langmuir waves.

Langmuir waves arise in the source regions of type III radio emissions. To study this kinetic instability, we will derive the general approach to obtaining the plasma dispersion relation. This will allow us to study the frequency and growth rate of waves in hot plasma.

The generality of the following approach lies within the way we obtain the plasma susceptibility $\overleftrightarrow{\chi}$. We will focus on obtaining the susceptibility tensor in this chapter. Using the susceptibility one can then determine the dispersion tensor $\mathcal{D}$ using equations (1.32) and (1.31). In order to determine the susceptibility we will first study the time evolution of the distribution function. We follow the derivation from [Stix, 1992, chapter 10] but we provide more detailed steps and use SI units.

Time evolution of the system

We represent our system using the phase space distribution function $f(\mathbf{r}, \mathbf{p}, t)$, introduced in section 1.3 (we switched from velocity to momentum coordinates for convenience). In the MHD approach, we only considered the moments of the phase space function, which can be obtained from f by integration. In the collisionless approach, we study the evolution of f in time.

In this chapter, we assume that f is the phase space distribution of one species. We can separate the problem this way because the susceptibility is additive over species, so at the end of our calculation we can simply sum over all species.

To study the time evolution of f, we will use the Boltzmann kinetic equation (1.5). We assume that the electromagnetic forces are the only long range forces acting upon the ionized particles, causing collective behavior of the plasma. Since we are dealing with weakly bound space plasma, we can neglect the collision term, obtaining the Vlasov equation

$$\frac{\partial f}{\partial t} + \mathbf{v} \cdot \frac{\partial f}{\partial \mathbf{r}} + q(\mathbf{E} + \mathbf{v} \times \mathbf{B}) \cdot \frac{\partial f}{\partial \mathbf{p}} = 0, \tag{1.37}$$

which provides the time evolution of f.

We can now split the phase space distribution function

$$f(\mathbf{r}, \mathbf{p}, t) = f_0(\mathbf{v}) + f_1(\mathbf{r}, \mathbf{p}, t), \tag{1.38}$$

where f_0 is the unperturbed zero order distribution function and f_1 is the first-order distribution function which can evolve with time. Similarly the electric field $\mathbf{E} = 0 + \mathbf{E_1}$ and the magnetic field $\mathbf{B} = \mathbf{B_0} + \mathbf{B_1}$.

If we now write the zero order Vlasov equation (plugging in the unperturbed field), for the unperturbed distribution function we get

$$\left(\frac{df_0}{dt}\right)_0 \equiv \frac{\partial f_0}{\partial t} + \mathbf{v} \cdot \frac{\partial f_0}{\partial \mathbf{r}} + q(\mathbf{v} \times \mathbf{B_0}) \cdot \frac{\partial f_0}{\partial \mathbf{p}} = 0, \tag{1.39}$$

where $\mathbf{v} = \frac{d\mathbf{r}}{dt}$ and $\mathbf{r}(t)$ is the trajectory of a particle traveling in the unperturbed field. This allows us to express the full Vlasov equation as

$$\left(\frac{df_1}{dt}\right)_0 = -q(\mathbf{E}_1 + \mathbf{v} \times \mathbf{B}_1) \cdot \frac{\partial f_0}{\partial \mathbf{p}}. \tag{1.40}$$

We can then integrate equation (1.40) in time to obtain the first order distribution

$$f_1(\mathbf{r}, \mathbf{v}, t) = -q \int_{-\infty}^{t} (\mathbf{E}_1(\mathbf{r}', t') + \mathbf{v}' \times \mathbf{B}_1(\mathbf{r}', t')) \cdot \frac{\partial f_0}{\partial \mathbf{p}'}\, dt', \tag{1.41}$$

where the prime denotes that we are integrating in time along the unperturbed trajectory $\mathbf{r}'(t')$.

In order simplify equation (1.40), we can assume an electric field decomposed to Fourier components in time and space

$$\mathbf{E}_1(\mathbf{r}', t') = \mathbf{E}(\omega) \exp(i\mathbf{k} \cdot \mathbf{r}' - i\omega t). \tag{1.42}$$

This assumption will also allow us to factor out the oscillatory term in the resulting time evoution of f_1 (obtained below in equation (1.59)), linearizing the problem.

Additionally we can express the magnetic field as $\mathbf{B}_1 = \frac{\mathbf{k}}{\omega} \times \mathbf{E}_1$. This allows us to simplify the term $\mathbf{v}' \times \mathbf{B}_1$ from equation (1.40) as

$$\mathbf{v}' \times \mathbf{B}_1 = \mathbf{v}' \times (\mathbf{k} \times \mathbf{E}) \frac{\exp(i\mathbf{k} \cdot \mathbf{r}' - i\omega t)}{\omega}, \tag{1.43}$$

omitting the oscillatory term $\frac{\exp(i\mathbf{k}\cdot\mathbf{r}' - i\omega t)}{\omega}$ we have

$$\begin{aligned}
\mathbf{v}' \times (\mathbf{k} \times \mathbf{E}) &= \epsilon_{ijk}\epsilon_{klm} v'_j k_l E_m \hat{\mathbf{e}}_i && (1.44)\\
&= (\delta_{il}\delta_{jm} - \delta_{im}\delta_{jl}) v'_j k_l E_m && (1.45)\\
&= E_m(\mathbf{v}'\mathbf{k})_{mi}\hat{\mathbf{e}}_i - E_m(\overleftrightarrow{\mathbf{1}})_{mi} v'_j k_j && (1.46)\\
&= \mathbf{E} \cdot (\mathbf{v}'\mathbf{k} - \overleftrightarrow{\mathbf{1}}\mathbf{v}' \cdot \mathbf{k}). && (1.47)
\end{aligned}$$

Substituting (1.47) to (1.41) we get

$$f_1(\mathbf{r},\mathbf{v},t) = -q\int\limits_{-\infty}^{t} \exp(i\mathbf{k}\cdot\mathbf{r}' - i\omega t')\mathbf{E}\cdot\left(\overleftrightarrow{\mathbf{1}}\left(1-\frac{\mathbf{v}'\cdot\mathbf{k}}{\omega}\right)+\frac{\mathbf{v}'\mathbf{k}}{\omega}\right)\cdot\frac{\partial f_0}{\partial\mathbf{p}'}\,dt'. \quad (1.48)$$

We will perform a substitution $\tau = t - t'$. Additionally, the unperturbed trajectory brings a few conditions which have to be met for the agreement of position and momenta at time $t' = t$:

$$\begin{aligned} v_x &= v_\perp\cos(\phi), & v_x' &= v_\perp\cos(\Omega\tau+\phi), & k_x &= k_\perp\cos(\theta),\\ v_y &= v_\perp\sin(\phi), & v_y' &= v_\perp\sin(\Omega\tau+\phi), & k_y &= k_\perp\sin(\theta),\\ v_z &= v_\parallel, & v_z' &= v_\parallel, & k_z &= k_\parallel, \end{aligned}$$

$$\begin{aligned} x' &= x - \frac{v_\perp}{\Omega}(\sin(\Omega\tau+\phi)-\sin(\phi)),\\ y' &= y - \frac{v_\perp}{\Omega}(\cos(\Omega\tau+\phi)-\cos(\phi))\\ z' &= z - v_\parallel\tau, \end{aligned}$$

where $\Omega = \frac{qB}{m}$ is the cyclotron frequency of the studied species.

Using these identities, we will convert to Cartesian coordinates starting with the term inside the exponential

$$\begin{aligned} \mathbf{k}\cdot\mathbf{r}' - \omega t' =& \mathbf{k}\cdot\mathbf{r} + \frac{v_\perp}{\Omega}k_\perp[(-\sin(\Omega\tau+\phi)-\sin(\phi))\cos(\theta)\\ &+(\cos(\Omega\tau+\phi)-\cos(\phi))\sin(\theta)] - v_\parallel k_\parallel\tau - \omega t + \omega\tau \quad (1.49)\\ =& \mathbf{k}\cdot\mathbf{r} - \omega t + \beta, \quad (1.50) \end{aligned}$$

where

$$\beta = (\omega - v_\parallel k_\parallel)\tau - \frac{v_\perp}{\Omega}k_\perp[\sin(\Omega\tau+\phi-\theta)+\sin(\phi-\theta)]. \quad (1.51)$$

Next we rewrite the derivative of f_0 in Cartesian coordinates as

$$\frac{\partial f_0}{\partial\mathbf{p}'} = \begin{bmatrix}\cos(\Omega\tau+\phi)\frac{\partial f_0}{\partial p_\perp}\\ \sin(\Omega\tau+\phi)\frac{\partial f_0}{\partial p_\perp}\\ \frac{\partial f_0}{\partial p_\parallel}\end{bmatrix}. \quad (1.52)$$

And lastly, we evaluate the tensor in equation (1.48), which we denote as

$$\overleftrightarrow{\mathbf{M}} = \left(\overleftrightarrow{\mathbf{1}}\left(1-\frac{\mathbf{v}'\cdot\mathbf{k}}{\omega}\right)+\frac{\mathbf{v}'\mathbf{k}}{\omega}\right). \quad (1.53)$$

On the diagonal we subtract

$$\mathbf{v}'\cdot\mathbf{k} = v_\perp k_\perp\cos(\Omega\tau+\phi)\cos\theta + v_\perp k_\perp\sin(\Omega\tau+\phi)\sin\theta + v_\parallel k_\parallel. \quad (1.54)$$

And the tensor product $\mathbf{v'k}$ is

$$\mathbf{v'k}=\begin{bmatrix} v_\perp k_\perp \cos(\Omega\tau+\phi)\cos\theta & v_\perp k_\perp \cos(\Omega\tau+\phi)\sin\theta & v_\perp k_\parallel \cos(\Omega\tau+\phi) \\ v_\perp k_\perp \sin(\Omega\tau+\phi)\cos\theta & v_\perp k_\perp \sin(\Omega\tau+\phi)\sin\theta & v_\perp k_\parallel \sin(\Omega\tau+\phi) \\ v_\parallel k_\perp \cos\theta & v_\parallel k_\perp \sin\theta & v_\parallel k_\parallel \end{bmatrix}, \tag{1.55}$$

allowing us to evaluate the entire matrix $\overleftrightarrow{\mathbf{M}}$. Using equations (1.54) and (1.55), we get

$$\overleftrightarrow{\mathbf{M}} = \begin{bmatrix} 1-\frac{v_\parallel k_\parallel}{\omega} & \frac{v_\perp k_\perp}{\omega}\cos(\Omega\tau+\phi)\sin\theta & \frac{v_\perp k_\parallel}{\omega}\cos(\Omega\tau+\phi) \\ -\frac{v_\perp k_\perp}{\omega}\sin(\Omega\tau+\tau)\sin\theta & & \\ \frac{v_\perp k_\perp}{\omega}\sin(\Omega\tau+\phi)\cos\theta & 1-\frac{v_\parallel k_\parallel}{\omega} & \frac{v_\perp k_\parallel}{\omega}\sin(\Omega\tau+\phi) \\ & -\frac{v_\perp k_\perp}{\omega}\cos(\Omega\tau+\tau)\cos\theta & \\ \frac{v_\parallel k_\perp}{\omega}\cos\theta & \frac{v_\parallel k_\perp}{\omega}\sin\theta & 1-\frac{v_\perp k_\perp}{\omega}\cos(\Omega\tau+\tau)\cos\theta \\ & & -\frac{v_\perp k_\perp}{\omega}\sin(\Omega\tau+\tau)\sin\theta \end{bmatrix}.$$

We can then we multiply $\overleftrightarrow{\mathbf{M}}$ by $\frac{\partial f_0}{\partial \mathbf{p}}$ which we obtained in equation (1.52):

$$\mathbf{E}\cdot\overleftrightarrow{\mathbf{M}}\cdot\frac{\partial f_0}{\partial \mathbf{p}} = \begin{bmatrix} E_x & E_y & E_z \end{bmatrix} \begin{bmatrix} \cos(\Omega\tau+\phi)\left(\frac{\partial f_0}{\partial p_\perp}\frac{k_\parallel}{\omega}\left(v_\perp\frac{\partial f_0}{\partial p_\parallel}-v_\parallel\frac{\partial f_0}{\partial p_\perp}\right)\right) \\ \sin(\Omega\tau+\phi)\left(\frac{\partial f_0}{\partial p_\perp}\frac{k_\parallel}{\omega}\left(v_\perp\frac{\partial f_0}{\partial p_\parallel}-v_\parallel\frac{\partial f_0}{\partial p_\perp}\right)\right) \\ \frac{\partial f_0}{\partial p_\parallel}+\cos(\Omega\tau+\phi)\frac{k_\perp}{\omega}\left(v_\parallel\frac{\partial f_0}{\partial p_\perp}-v_\perp\frac{\partial f_0}{\partial p_\parallel}\right) \end{bmatrix}. \tag{1.56}$$

To simplify these terms, we define

$$U = \left(\frac{\partial f_0}{\partial p_\perp}\frac{k_\parallel}{\omega}\left(v_\perp\frac{\partial f_0}{\partial p_\parallel}-v_\parallel\frac{\partial f_0}{\partial p_\perp}\right)\right) \tag{1.57}$$

$$V = \frac{k_\perp}{\omega}\left(v_\parallel\frac{\partial f_0}{\partial p_\perp}-v_\perp\frac{\partial f_0}{\partial p_\parallel}\right). \tag{1.58}$$

Plugging these results into equation (1.48) and performing the substitution $\tau = t - t'$ ($dt' = -d\tau$), we obtain

$$\begin{aligned} f_1(\mathbf{r},\mathbf{p},t) = -q\exp(i\mathbf{k}\cdot\mathbf{r}-i\omega t)\int_0^\infty \exp(i\beta)[E_x\cos(\Omega\tau+\phi)U \\ +E_y\sin(\Omega\tau+\phi)U + E_z\left(\frac{\partial f_0}{\partial \mathbf{p}_\parallel}+\cos(\Omega\tau+\phi)V\right)]d\tau. \end{aligned} \tag{1.59}$$

We have thus derived a formula for the time dependent perturbed velocity distribution function, providing us with the time evolution of the system.

Hot plasma susceptibility

To determine the susceptibility $\overleftrightarrow{\chi}$, we need to determine the conductivity $\overleftrightarrow{\sigma}$. From equations (1.32) and (1.33), we can rewrite the problem as

$$\mathbf{j} = \sum_s q_s \int v_s f_{s1} d^3p = -i\omega\epsilon_0 \sum_s \overleftrightarrow{\chi}_s \cdot \mathbf{E}_1. \tag{1.60}$$

Since the susceptibility is additive over particle species, we can obtain the contributions for each species individually. For a single species, we can write

$$\overleftrightarrow{\chi} \cdot \mathbf{E}_1 = \frac{iq}{\omega\epsilon_0 m} \iiint \mathbf{p} f_1(\mathbf{r}, \mathbf{p}, t) d^3p, \tag{1.61}$$

where $\mathbf{p} = \begin{bmatrix} p_\perp \cos(\phi) \\ p_\perp \sin(\phi) \\ p_\parallel \end{bmatrix}$, and $d^3p = p_\perp d\phi dp_\perp dp_\parallel$.

Focusing on the first component $(\overleftrightarrow{\chi} \cdot \mathbf{E}_1)_x$ is now equivalent to replacing $\mathbf{p}$ with $p_\perp \cos(\phi)$ in equation (1.61). Furthermore, f_1 was obtained by doing the scalar product with $\mathbf{E}_1$, so by only considering the term multiplied by E_{1x} we can determine χ_{xx}.

Following this procedure analogously for all components of $\mathbf{p}$ and $\mathbf{E}_1$ would provide us with the full susceptibility tensor. For the sake of brevity, we will only focus on the first term.

Writing out f_1 we split $e^{i\beta}$ into two factors, one depending on ϕ and the other one independent of ϕ. We also substitute $z = \frac{k_\perp v_\perp}{\Omega}$ to simplify the integral

$$\begin{aligned} \chi_{xx} = \frac{-iq^2}{\omega\epsilon_0 m} \int_{-\infty}^{\infty} p_\perp \int_{-\infty}^{\infty} U \int_0^{\infty} \int_0^{2\pi} \cos(\phi) e^{-iz(\sin(\Omega\tau+\phi)-\sin(\phi))} \\ \cdot \cos(\Omega\tau + \phi) d\phi e^{i(\omega - v_\parallel k_\parallel)\tau} d\tau dp_\parallel dp_\perp. \end{aligned} \tag{1.62}$$

We will start by performing the inner integral over the azimuthal angle ϕ. We can use the Jacobi-Anger expansion

$$e^{iz\sin(\phi)} = \sum_{n=-\infty}^{\infty} e^{in\phi} J_n(z) \tag{1.63}$$

to evaluate the integral. Differentiating (1.63) with respect to ϕ gives us

$$\cos(\phi) e^{iz\sin(\phi)} = \sum_{n=-\infty}^{\infty} ine^{in\phi} J_n(z) \tag{1.64}$$

Performing a substitution $\phi \to (\Omega\tau + \phi)$ gives us

$$\cos(\Omega\tau + \phi) e^{iz\sin(\Omega\tau+\phi)} = \sum_{n=-\infty}^{\infty} ine^{in(\Omega\tau+\phi)} J_n(z). \tag{1.65}$$

Now we can multiply equations (1.64) and (1.65), obtaining

$$\begin{aligned} z^2\cos(\phi)\cos(\Omega\tau+\phi)e^{-iz(\sin(\Omega\tau+\phi)-\sin(\phi))} &= \\ &= \left(\sum_{n=-\infty}^{\infty} -ine^{-in\phi}J_n(z)\right)\left(\sum_{n=-\infty}^{\infty} ine^{in(\Omega\tau+\phi)}J_n(z)\right) \\ &= \sum_{n=-\infty}^{\infty} n^2 e^{in\Omega\tau}J_n^2(z), \end{aligned} \tag{1.66}$$

where we could multiply the sums due to the orthogonality of Bessel functions.

After dividing by z^2 we can perform the integration in ϕ. The left hand side of equation (1.66) allows us to evaluate the inner most integral from equation (1.62). We evaluate it by integrating the right hand side of equation (1.66). Since it is independent of ϕ the integration is trivial, obtaining the inner most integral as

$$\int_0^{2\pi} \cos(\phi)\cos(\Omega\tau+\phi)e^{-iz(\sin(\Omega\tau+\phi)-\sin(\phi))}d\phi = 2\pi\sum_{n=-\infty}^{\infty}\frac{n^2}{z^2}J_n^2(z)e^{in\Omega\tau}. \tag{1.67}$$

We can now plug in this result into equation (1.62) and integrate in time:

$$\chi_{xx} = 2\pi\frac{-iq^2}{\omega\epsilon_0 m}\int_{-\infty}^{\infty} p_\perp \int_{-\infty}^{\infty} U \sum_{n=-\infty}^{\infty}\frac{n^2}{z^2}J_n^2(z)\int_0^{\infty} e^{i(n\Omega+\omega-v_\parallel k_\parallel)\tau}d\tau dp_\parallel dp_\perp \tag{1.68}$$

$$= 2\pi\frac{-iq^2}{\omega\epsilon_0 m}\sum_{n=-\infty}^{\infty}\int_{-\infty}^{\infty} p_\perp\frac{n^2}{z^2}J_n^2(z)\int_{-\infty}^{\infty}\frac{U}{\omega - v_\parallel k_\parallel - n\Omega}dp_\parallel dp_\perp. \tag{1.69}$$

Now we have the susceptibility component χ_{xx} expressed using the unperturbed distribution f_0 (which lies within the term U).

When performing the calculation for other components, similar tricks (differentiation with respect to ϕ or τ) with the Jacobi-Anger expansion provide a way to integrate over ϕ.

In the end we get an integral over the parallel and perpendicular momenta which involves terms with first derivatives of f_0 with respect to the momentum. Provided we know the phase space distribution function for each species we can calculate these derivatives and perform the integration. This can be done numerically for each n in the sum until the contribution becomes sufficiently small. Performing this calculation and summing over the species gives us the full susceptibility tensor.

This approach is used in numerical plasma dispersion relation solvers, such as the Arbitrary Linear Plasma Solver (ALPS) by Klein et al. [2023].

2. Type III radio emissions

This chapter offers a comprehensive review of type III radio emissions. These radio bursts are generated by energetic electrons which are ejected from the Sun and travel within the solar wind. These emissions are often associated with powerful solar phenomena, such as coronal mass ejections (CMEs).

Following their origin from the Sun, energetic electron beams propagate away from the Sun, traveling along the magnetic field lines. The electron beam interacts with the solar wind along its path, causing Langmuir waves to grow.

Since Langmuir waves cannot propagate over large distances, they can only be observed in situ. However, they can undergo mode conversion, transforming the Langmuir waves into radio emissions at the plasma frequency or its first harmonic.

This resulting radio emission, known as a Type III radio emission, propagates in the free space mode and can thus be remotely observed by spacecraft or partially through ground-based observations. However, the ground based observations are limited by the ionosphere cutoff frequency ($5 - 8$MHz [Gurnett and Bhattacharjee, 2017, page 135]).

2.1 Beam driven instability

The collisionless approach can be used to investigate the interaction of an electron beam with the background solar wind. As derived in chapter 1, given the velocity distribution functions of all plasma species, one can determine the stability of the system and the growth rate of plasma waves.

To execute the stability analysis of velocity distribution functions (VDFs), we need to obtain a model of the system at hand. Direct instrumental observations will then provide us the necessary data to fit the parameters of our model. In the following section we introduce possible models of the background VDF.

2.1.1 Analytical models

Analytical models of velocity distribution functions play a key role in space particle physics. They allow us to characterize the velocity distribution function of each species with a few parameters. The fit parameters also often have a clear physical interpretation, such as the temperature (T) or drift velocity ($\mathbf{U}$).

Even non-physical models such as cubic splines and generalized additive models can be applied in modeling velocity distribution functions. These models can sometimes be easier to use, but their parameters do not provide much insight to the physics at hand.

We begin by reviewing analytical models, which can be derived from statistical mechanics. In the simplest model of an electron VDF, we assume thermodynamic equilibrium, leading to the Maxwell-Boltzmann distribution. We write

our VDFs in field aligned momentum coordinates because this form is most convenient for evaluating the integral (1.68) (and other components of $\overleftrightarrow{\chi}$). We can also assume that our drift velocity $\mathbf{U}$ is field aligned. For the Maxwellian VDF we get

$$f(p_\parallel, p_\perp; w_\parallel, w_\perp, U) = \frac{1}{\pi^{3/2} m^3 w_\parallel v_\perp^2} \exp\left(-\frac{p_\perp^2}{m^2 w_\perp^2} - \frac{(p_\parallel - mU)^2}{m^2 w_\parallel^2}\right), \tag{2.1}$$

where the thermal velocities w parallel and perpendicular to $\mathbf{B}$ are

$$w_\parallel = \sqrt{\frac{2k_B T_\parallel}{m}}, \tag{2.2}$$

$$w_\perp = \sqrt{\frac{2k_B T_\perp}{m}}. \tag{2.3}$$

We can use equation (2.1) to describe any species of particles. Using equation (2.1) to fit experimental measurements allows us to determine the temperature and bulk speed of the electron population.

However, space plasmas in the state of thermodynamic equilibrium are rarely observed. The issue with our model is that the Gibbs-Boltzmann statistical mechanics assumes a high number of collisions. That argument holds well for gasses, but not generally for all space plasmas. In space plasmas, collisions often have a negligible effect, meaning that the system does not reach thermodynamic equilibrium.

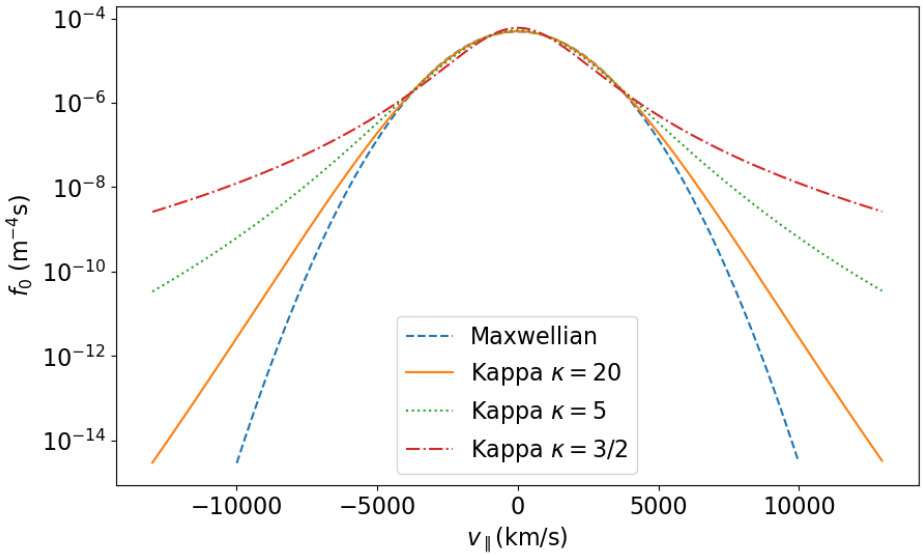

Figure 2.1: A comparison of the Maxwellian and Kappa reduced distribution functions for $T_e = 140000$ K.

A different approach is required to account for the collective behavior. By the means of non-extensive statistical mechanics, a generalized model of VDFs in space plasmas can be derived, as shown by Livadiotis and McComas [2013].

This derivation yields a generalized Maxwellian distribution, commonly regarded as the Kappa distribution. Again, we convert the result of this derivation to our field aligned momentum coordinates, obtaining

$$f(p_\parallel, p_\perp; w_\parallel, w_\perp, U, \kappa) = \frac{1}{\pi^{3/2} m^3 w_\parallel w_\perp^2} \left(\frac{2}{\pi(2\kappa-3)}\right)^{3/2} \frac{\Gamma(\kappa+1)}{\Gamma(\kappa-1/2)} \cdot \left(1 + \frac{2}{2\kappa-3}\left[\frac{p_\perp^2}{m^2 w_\perp^2} + \frac{(p_\parallel - mU)^2}{m^2 w_\parallel^2}\right]\right)^{-(\kappa+1)}. \tag{2.4}$$

Where $\kappa \in (\frac{3}{2}, \infty)$ is the kappa parameter of the distribution. The value of κ tells us how far we are from thermal equilibrium. In the limit $\kappa \to \infty$ the Kappa distribution converges to the Maxwellian, as demonstrated in figure 2.1.

In figure 2.1 we are showing the reduced VDF, which can be obtained from the full VDF by integrating along the perpendicular velocities. The reduced VDF can be used to investigate the stability of the system, as shown in [Gurnett and Bhattacharjee, 2017, chapter 9.5]. Notably, a positive slope in the reduced VDF is a necessary but not sufficient condition for instability.

The Kappa distribution (2.4) allows us to describe stationary states outside of thermodynamic equilibrium. As demonstrated by Maksimovic et al. [1997], the Kappa distribution can be used to model the electron VDF in the fast solar wind, capturing its characteristic high-velocity tails.

2.1.2 Multiple populations

So far, we have been describing the background VDF. However, in order to study type III radio emissions, we must also include the electron beam population. The electron beam propagation has been studied by the means of numerical simulations by Kontar and Reid [2009]. They showed that the high energy electrons in the beam lose their energy to the plasma waves and this energy is then reabsorbed by the lower energetic electrons in the beam. Although this mechanism is not yet well theoretically understood, it allows for the beam to propagate over large distances.

Another way to study the electron VDF introduces multiple populations of electrons:

- Thermal core - A Maxwellian VDF describing $\sim 95\%$ of the number density.
- Halo - A suprathermal population of electrons exhibiting a power-law behavior at high energies. This tail of the electron VDF can be modelled by the Kappa distribution.
- Strahl - An anisotropic field aligned population of electrons appearing as a shoulder on the electron VDF.
- Electron beam - A separate population of electrons with a large bulk velocity ($\sim$ 10keV) directed anti-Sun-ward.

This approach of using different electron populations has been used by Verscharen et al. [2022] to describe the kinetic instabilities that can arise from the electron VDF.

2.2 Wave modes

During in situ type III radio emissions, a passing electron beam causes the growth of plasma waves. In this section we overview the available wave modes which are relevant for studying the source regions of type III radio emissions.

2.2.1 Langmuir mode

Langmuir waves are longitudinal pressure waves at or above the local electron plasma frequency. They cause rapid oscillations in the plasma electron density.

The dispersion relation of Langmuir waves is called the Bohm-Gross dispersion relation. The dispersion relation provides a formula for the frequency of the Langmuir wave

$$\omega^2 = \Pi_{pe}^2(1 + \gamma_e \lambda_{De}^2 k^2), \tag{2.5}$$

where Π_{pe} is the electron plasma frequency, γ_e is the power law index ($\gamma_e = 3$ for longitudinal waves one-dimensional compression), λ_{De} is the Debye shielding length and k is the magnitude of the wave vector. The Bohm-Gross dispersion (derived in Gurnett and Bhattacharjee [2017]) holds true for $k\lambda_{De} \ll 1$. For higher values of $k\lambda_{De} \geq 1$, Langmuir waves cannot propagate far due to Landau damping.

An intuitive understanding of Landau damping can be obtained by considering the situation of a monotonously decreasing VDF. At any point there are more particles that are slower than the phase velocity of the wave and interaction with the wave causes the wave to lose energy to the acceleration of these particles.

An analogous process can be used to explain the Langmuir wave growth when a bump in the VDF is present. At the bump, there is temporarily more particles faster than the wave phase velocity, which causes the growth of the wave and flattens the VDF, creating a plateau.

2.2.2 Z-Mode

The Z-mode is a continuously connected branch of the index of refraction which can be derived in the cold plasma approach (see Gurnett and Bhattacharjee [2017]). It is a perpendicularly polarized electromagnetic wave.

The solution for the allowed wave modes varies as we move above or below the local plasma frequency. When we are above the plasma frequency and below the upper hybrid frequency ($\omega_{UH} > \omega > \Pi_p$), only the X mode is accessible. Thus we have a resonance at some angle between the $\mathbf{k}$ vector and the magnetic field. This means that above the plasma frequency the Z-mode cannot propagate directly along the magnetic field.

Below the plasma frequency, the Z-mode can also exist up until the L-cutoff frequency ($\Pi_p > \omega > \omega_L$). In this region both the L and X mode are accessible for the Z-mode, meaning that the wave can propagate in any direction.

2.3 Previous studies

The first observations of type III radio emissions were presented by Wild [1950], exhibiting a characteristic drift in frequency of the radio emission with time. The proposed explanation for the frequency drift was a drifting source of the radio emission.

With the increasing access to space, this explanation was tested by spacecraft observations. Using data from the IMP mission Gurnett and Frank [1975] showed the observation of an in situ type III radio event at 1 AU. With observations performed closer to the Sun, Gurnett and Anderson [1976] presented the association of Langmuir waves with type III radio emissions as observed by the Helios 1 spacecraft. Type III radio emission can be observed at a wide range of heliospheric distances, as shown by the Cassini's observations at 10 AU [Boudjada et al., 2020].

The effects of density inhomogenities on Langmuir wave generation were studied using ISEE 3 data by Robinson et al. [1992]. They show that Langmuir waves often appear in clumps, which corresponds to density fluctuations in the solar wind. The effect of density inhomogenities on the fundamental radio emission was investigated by Krupar et al. [2018] using the STEREO spacecraft, showing that the decay profile of type III bursts can be explained by the scattering of the fundamental component between the source and the observer.

The mechanism behind the radio wave generation has been a subject of study since the late 1950s. The conversion process from Langmuir waves to radio waves at the plasma frequency and its second harmonic was studied by Zheleznyakov and Zaitsev [1970], Melrose [1980] and more recently Jebaraj et al. [2023] (and references therein). The generally accepted understanding is that the generated Langmuir waves decay and due to nonlinear wave interaction produce the radio emission.

Additionally, the type III radio emissions have been studied theoretically by modeling the electron beam and its interaction with the solar wind. The evolution of the electron beam population was studied by Kontar and Reid [2009], Reid and Kontar [2012] and Lorfing et al. [2023], predicting a spectral break in the electron velocity distribution. Furthermore Lorfing and Reid [2023] predicted the electron beam velocities which allow for Langmuir wave growth.

For a more exhaustive overview of type III radio emissions see Reid et al. [2014].

3. The Solar Orbiter spacecraft

The Solar Orbiter spacecraft was developed by the European Space Agency. The spacecraft launched in February 2020 from Cape Canaveral and is equipped with scientific instruments dedicated to studying the Sun and the solar wind environment.

This section provides a brief overview of the onboard instruments, which are used for observing in situ type III events. These instruments (highlighted on figure 3.1) include the Radio and Plasma Waves (RPW) instrument for the wave observations, the Solar Wind Analyzer (SWA) and the Energetic Particle Detector (EPD) instruments for electron beam observations and the Magnetometer (MAG) instrument for magnetic field observation.

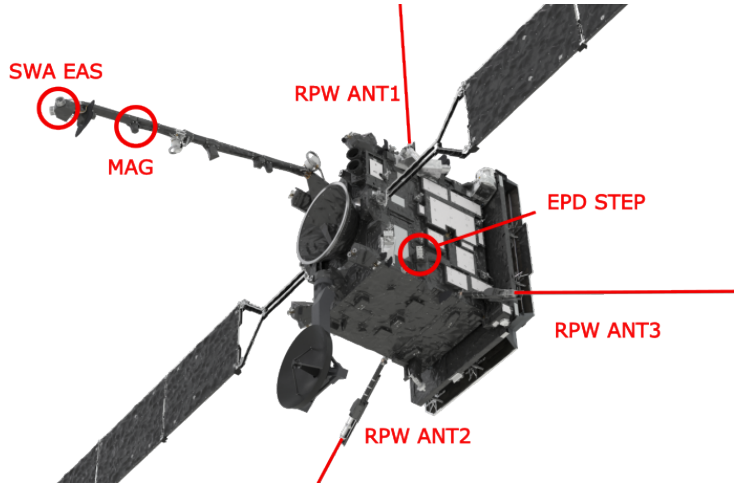

Figure 3.1: A visualization of the Solar Orbiter spacecraft highlighting the onboard instruments used for observing in situ type III events. Image source: [ESA/ATG MediaLab, 2019]

3.1 The Spacecraft Reference Frame

Several instruments described in the next section have their own coordinate system, typically aligned with the symmetries and orientation of the sensors. However, when analyzing data from multiple instruments, it is convenient to establish a common reference frame. The Spacecraft Referece Frame (SRF) allows us to directly compare measurements between the instruments.

The SRF axes are shown in figure 3.2. The SRF X-axis points towards the Sun and the Y-Z plane is aligned with the electric antennas.

The data files from the particle instruments onboard usually contain a coordinate transformation matrix which we use to convert the data to the SRF. For the electric waveform data, we convert to the SRF by using the antenna effective lengths.

3.2 Description of instruments

3.2.1 Radio and Plasma Waves

The Radio and Plasma Waves (RPW) instrument [Maksimovic et al., 2020] provides measurements of the electric and magnetic field waves. All of the RPW subsystems are conencted to the three electric antennas. We will focus on the Time Domain Sampler (TDS) subsystem since it provides the ability to observe both the in-situ Langmuir waves and the type III radio emission.

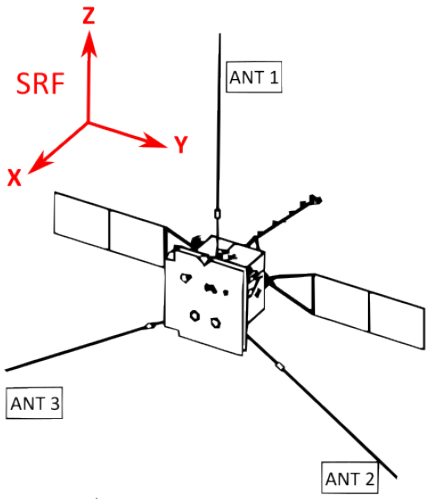

Figure 3.2: A visualization of the Spacecraft Reference Frame (SRF) axes.

Time Domain Sampler (TDS)

The TDS receiver covers a frequency range from 200 Hz up to 200 kHz and has four channels, which are connected to the three electric antennas and the search coil magnetometer. In the usual configuration, the TDS measures two electric components in dipole mode, one component in monopole and the magnetic field waveform data in the fourth channel. The TDS produces several data products which we can use to observe Langmuir waves.

The TDS measures one waveform snapshot each second, covering ∼62.5 ms (6.25% of the time) of the second, typically at the sampling frequency of 262 kHz. All of the waveform snapshots are then labeled by the onboard algorithm (wave emission, dust impact, and other triggers). The algorithm is also responsible for choosing which waveforms are saved, producing the triggered waveform data product (TSWF). These snapshots facilitate our Langmuir wave detection capabilities.

Additionally, the regular waveform data (RSWF) consist of snapshots saved regularly, typically at 5-minute intervals. This data product provides an overview of entire type III events, showing the radio emissions and the Langmuir waves.

And lastly, the MAximum AMplitude data (MAMP) is a continuously sampled data product at the rate of 2097.1 ksps, with the maximum amplitude values

being stored every 7.8-250 ms. Despite potential spacecraft interferences, MAMP data allows for tracking wave packets of Langmuir waves.

The TDS can be operated in multiple modes which determines parameters such as the sampling frequency, how many snapshots get saved by the algorithm or how often the regular snapshots are saved. For observing type III radio emissions, there is a special mode called the SBM2 mode. This Selected Burst Mode can be triggered by an onboard algorithm which performs a real time analysis of the spacecraft observations. When triggered, this mode increases the number of saved triggered waveforms, which allows for more Langmuir wave observations.

To improve the TDS's performance, we have performed an analysis of the onboard algorithm which triggers the SBM2 mode. This analysis resulted in better performing set of parameters which are tuned so that more type III emissions are detected. These parameters have been uploaded to the Solar Orbiter spacecraft and in use since July 2021.

3.2.2 Solar Wind Analyser

The Solar Wind Analyser (SWA) instrument consists of several systems, each dedicated to analyzing different populations of particles in the solar wind. These systems and the science motivations behind the instrument are described in detail by Owen et al. [2020]. For the purpose of our study of the electron VDF, we describe the measurement principle of the Electron Analyser System (EAS) and its associated data products.

The Electron Analyser System (EAS)

The EAS system consists of two top-hat electrostatic analyzers (EAS1 and EAS2). They are mounted orthogonaly to each other on the end of the spacecraft boom, as shown in figure 3.1.

First, the electrons arriving at either sensor head are deflected into the electron analyzer by applying a positive charge to the external deflector electrodes (part of the Aperture Deflection System - ADS). Each head has two such electrodes, to control the acceptance angle, providing 16 elevation bins.

Inside the electron analyzer, the electrons are guided using another pair of deflector electrodes, which allows for the determination of the electron energy. These deflectors allow for a resolution of 64 energy levels at each elevation.

Then the electrons arrive at the detector and readout element. For the detection a multichannel detector plate is used. The detector has 32 bins, providing azimuthal resolution by splitting the 360° azimuth acceptance angle.

As a result, each analyzer head provides 16 elevation bins ($\pm 45°$), 32 azimuthal bins (360°), and 64 energy level bins (from 1eV to 5keV) for each measured direction. The entire measurement process includes 16 sweeps in energy for each elevation and takes $\sim$ 1s to complete. Combining the fields of view of both instrument heads provides a full 4π steradian 3D VDF. Although it is important to note that certain directions are obscured by the spacecraft, its solar panels and

some structural elements of the instrument heads.

The 1s 3D VDF data from the EAS1 and EAS2 heads has a 10s cadence in the normal mode and a 1s cadence in the triggered mode.

3.2.3 The Energetic Particle Detector

The Energetic Particle Detector (EPD) allows Solar Orbiter to observe electrons at suptrathermal energies. These energies play a crutial role when growing Langmuir waves as investigated by Lorfing and Reid [2023]. We describe the electron sensors of EPD which can be used to observe electron beams generating for type III radio emissions.

The SupraThermal Electron Proton sensor (STEP)

The STEP sensor (detailed description in Rodríguez-Pacheco et al. [2020]) measures protons and electrons at suprathermal energies of $7\ \text{keV} - 80\ \text{keV}$. This detector consists of two sensor heads with an aligned field of view, where one of the sensors contains a permanent magnet to deflect electrons. The sensor head with the permanent magnet (magnet channel) thus only measures ions and the other sensor head measures both electrons and ions (integral channel). We can obtain the electron observations from the STEP detector by subtracting the magnet channel from the integral channel data.

The two sensor heads of STEP have a field of view of $28° \times 54°$ aligned with the nominal Parker spiral. The wider angle being in the ecliptic plane. The sensors use a pinhole design and a segmented solid state detector to achieve spacial resolution.

The segmented solid state sensor is made from two identical silicon semiconductor diode detectors. When a particle impacts the diode detector, it allows current to flow. Each of the segmented sensors consists of 15 segments in a 3×5 array and one segment[1] for background noise correction.

The maximum time resolution of the STEP measurement is 1s, with the duty cycle of the solid state detector being 100%.

The Electron Proton Telescope (EPT)

This sensor is designed to measure electrons with energies of $25\,\text{keV} - 475\,\text{keV}$ and protons with energies of $25\,\text{keV} - 6.4\,\text{MeV}$. The EPT consists of two units, each unit having two double-ended telescopes with a 30° field of view in opposite directions. The maximum time resolution of the EPT electron and proton measurements is 1 s.

The two units give a total of four fields of view, one being in the Sun and anti-Sun direction and the other looking northward and southward. The instrument design, described in greater detail in Rodríguez-Pacheco et al. [2020], uses a magnet/foil design derived from the STEREO/SEPT instrument (Müller-Mellin et al. [2008]).

[1] Shielded by an aluminum lid to prevent particles from reaching this segment.

Each double-ended telescope has two apertures in opposite directions. One aperture contains a thin foil to stop ions (below $\sim 400\,\mathrm{eV}$) and lets electrons pass through. The other aperture contains a magnet which deflects the electrons leaving only ions to reach the sensor. The sensor used in EPT is a back-to-back mounted, segmented, silicon based solid state detector.

3.2.4 Magnetometer

The Solar Orbiter Magnetometer (MAG), described in detail by Horbury et al. [2020], is a scientific instrument designed to measure the magnetic field around the Sun with high precision. This magnetometer utilizes a dual fluxgate design, meaning it has two separate sensors for redundancy and to differentiate between the magnetic field of the spacecraft and the Sun itself.

The two sensors are located on the spacecraft boom, remaining in the shadow. To maintain a stable sensor temperatures there are redundant thermistors and a heating element, which keeps the sensors above the minimum operational temperature of $-100\,^{\circ}\mathrm{C}$.

The instrument then amplifies the signal, filters it, and converts it into digital data. The instrument can operate in different ranges depending on the strength of the magnetic field. The data is then sent to the spacecraft for further processing and transmission to Earth.

We use the ambient magnetic field measurement by MAG to convert measurements done by other instruments into field aligned coordinates. The MAG data used in our analysis has a cadence of 8 vectors/s.

Data Analysis Objectives

Having established a comprehensive theoretical foundation in the preceding chapters, we outline the specific objectives of this thesis. The in situ observations by the Solar Orbiter spacecraft allow us to analyze the source regions of type III radio emissions.

Our focus lies on the interaction of the electron beam with the solar wind and the generation and characteristics of Langmuir waves:

- Using the electron observations performed by the Solar Orbiter spacecraft, we will develop a model of the electron velocity distribution.
- We will employ the Poisson maximum likelihood method to accurately determine the model parameters, thereby extracting the key features that define the electron velocity distribution function.
- For the modeled velocity distributions, we will determine its stability and the possibility of Langmuir wave growth. This will be achieved by employing numerical methods, specifically the ALPS plasma dispersion relation solver. By obtaining the dispersion relation, we aim to gain a deeper understanding of the plasma instabilities within the solar wind.
- We will also conduct a Hilbert transform analysis of observed electric waveforms from the Solar Orbiter. This analysis will allow us to determine the characteristics of observed plasma waves, focusing on their frequency distribution and polarization.

By addressing these objectives, the presented thesis aims to contribute to the broader understanding of type III radio emission generation in the solar wind environment and provide insights into the mechanisms driving the Langmuir wave growth.

4. Analysis of kinetic instabilities caused by the electron beam

The hot plasma dispersion relation method described in chapter 1 allows us to study the stability of electron VDFs in the solar wind. In this chapter we describe how the electron VDF can be obtained from measurement data and how we can use it to run the ALPS code to solve the dispersion relation.

4.1 Observed electron distributions

For our analysis, we use the data from both the SWA-EAS sensor and the EAS-STEP data. Together, these data products cover the velocities which are relevant for Langmuir wave growth.

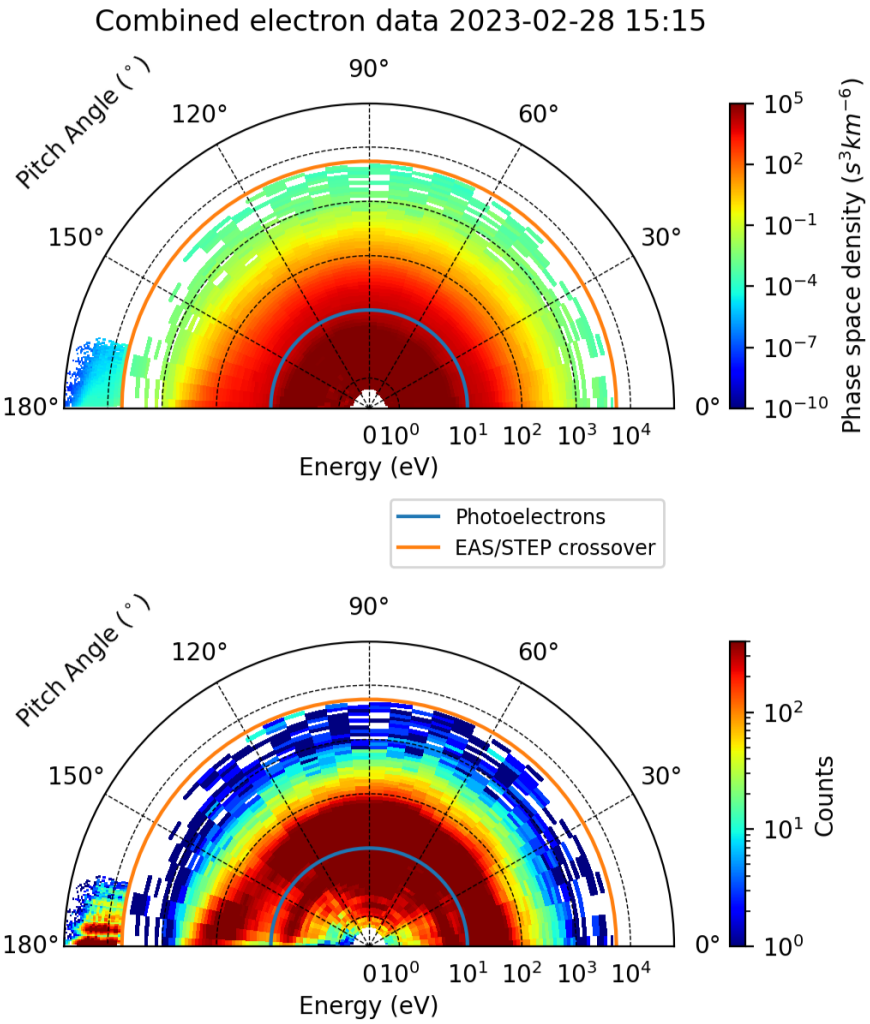

Figure 4.1: A time averaged electron pitch angle distribution from SWA-EAS (600 s average) below 5 keV and EPD-STEP (60 s average) above 7 keV. The blue lines highlights the energy threshold for photoelectrons induced by the spacecraft potential and the orange line signifies the crossing between EAS and STEP energies.

For our analysis, we need to obtain the VDF in the field aligned momentum coordinates. To achieve this, we transform the EAS phase space density data from the EAS coordinate system to SRF. Then, we can project each pixel onto the magnetic field direction. Additionally, we remove all the pixel look directions which are obscured by the spacecraft (solar panels, EAS support pillars).

After the transformation we have an irregular grid with coordinates $(p_\parallel, p_\perp)$. The phase space density is also accompanied by the raw count data. We then transform the EAS data to a regular energy - pitch angle grid with an angular resolution of 36 pitch angles covering the full range of $(0°, 180°)$. We average the phase space density values within the grid points and sum the raw counts.

For the STEP data an analogous approach is used to obtain a second regular grid with the phase space density and counts at suprathermal energies. The result of this transformation are shown in figure 4.1.

Having created a regular grid in the energy-pitch angle space, we still need to convert the data to a regular grid in $(p_\parallel, p_\perp)$ coordinates[1].

4.2 Model of the velocity distribution

Using the Maxwellian (2.1) and Kappa (2.4) distributions, we can fit the pitch angle distribution data and then use the fit parameters to generate a regular grid in $(p_\parallel, p_\perp)$ coordinates.

4.2.1 Maximum likelihood method

Our electron observations obey the Poisson distribution. This makes the least squares minimization method inaccurate. In order to obtain the correct fit parameters for our model we perform a maximization of the Poisson probability according to a method developed by Santolik [1995]

$$P = \Pi_{i=1}^{m} p(N_i), \tag{4.1}$$

where m is the number of observations, and $p(N_i)$ is the probability of observing N_i counts for given parameters. This probability is given by the Poisson distribution

$$p(N_i) = \frac{e^{n_i} n_i^{N_i}}{N_i!}, \tag{4.2}$$

where the parameter n_i is the predicted count.

For convenience, we will be minimizing the function

$$\mu(\mathbf{a}) = -\ln(P) = \sum_{i=1}^{m} \ln(p(N_i), \tag{4.3}$$

[1]We note that it is convenient to first perform the pitch angle transformation as it allows for simple data visualization and if we keep the count information we can still perform accurate data analysis and fitting. However, it should be possible to perform the fitting directly on the irregular $(p_\parallel, p_\perp)$ grid.

which is equvalent to maximizing the likelihood P. Plugging (4.1) into (4.3) we obtain

$$\mu(\mathbf{a}) = \sum_{i=1}^{m} \ln\left(\frac{e^{-n_i} n_i^{N_i}}{N_i!}\right) \tag{4.4}$$

$$= \sum_{i=1}^{m} n_i - N_i \ln(n_i) + \ln(N_i!). \tag{4.5}$$

Since the term $\ln(N_i!)$ does not depend on the fit parameters $\mathbf{a}$, the parameter optimization can be performed using the function

$$\mu^*(\mathbf{a}) = \sum_{i=1}^{m} n_i - N_i \ln(n_i). \tag{4.6}$$

4.2.2 Determination of the model parameters

As shown in figure 4.1, we have both the phase space density and count data for each pitch angle and energy. We can determine the count coefficients for each data point, which allows us to convert the fit result to the predicted counts n_i. Performing this fit this way allows for the count uncertainty of each data point to be considered.

For this investigation we chose the electron observations recorded on February 28$^{\text{th}}$ 2023 at 15:15, shown on figure 4.1. For our fit we chose a Maxwellian distribution to describe the thermal core, a Kappa distribution corresponding to the halo and strahl population and lastly a second Maxwellian distribution to describe the electron beam:

$$\begin{aligned} f_{fit}(\widetilde{p_\parallel}, \widetilde{p_\perp}; \mathbf{a}, \mathbf{b}, \mathbf{c}, \mathbf{d}, \mathbf{e}) = a_1 \exp(-b_1(\widetilde{p_\parallel} - c_1)^2 - b_1 d_1 \widetilde{p_\perp}^{\,2}) \\ +a_2(1 + [b_2(\widetilde{p_\parallel} - c_2)^2 + e_2 \widetilde{p_\perp}^{\,2}])^{d_2} + a_3 \exp(-b_3(\widetilde{p_\parallel} - c_3)^2 - b_3 d_3 \widetilde{p_\perp}^{\,2}). \end{aligned} \tag{4.7}$$

The resulting fit is shown in figure (4.2) and the fit parameters are listed in table 4.1. In the fit, we excluded the measurements below 15 eV which correspond to photoelectrons. This effect is caused by the presence of the spacecraft and artificially increases the flux of low energy particles.

	Core (1)	Halo+Strahl (2)	Beam (3)
a	0.0698	0.0152	6.13e-10
b	12.8	2.56	0.0971
c	0.0297	-0.212	-10.9
d	0.78	-3.56	30.6
e	-	8.12	-

Table 4.1: Raw fit parameters of the normalized distribution.

Our model, described by equation (4.7), was chosen because superposing Maxwellians and a Kappa distribution allows us to use the fit results to run

ALPS. A more complex model of the electron VDF as used by Štverák et al. [2009] could provide physical parameters which better describe the system. The limitations of our model can be seen when we consider the relative densities n_r of the populations, listed in table 4.2.

	Core	Halo+Strahl	Beam
n_r	0.860	0.140	$2.91 \cdot 10^{-7}$
$T_\parallel$	11.1 eV	52.3 eV	1.46 keV
$T_\perp$	14.2 eV	16.5 eV	47.6 eV
U	0.125 eV	6.38 eV	16.7 keV
κ	-	2.56	-

Table 4.2: Physical parameters of the fitted distribution.

From the physical parameters in table 4.2, we see that the electron beam energy is 16.7 eV. We also see the drift of the strahl population and the temperature anisotropies caused by the presence of a magnetic field of $B \approx 18.5$ nT.

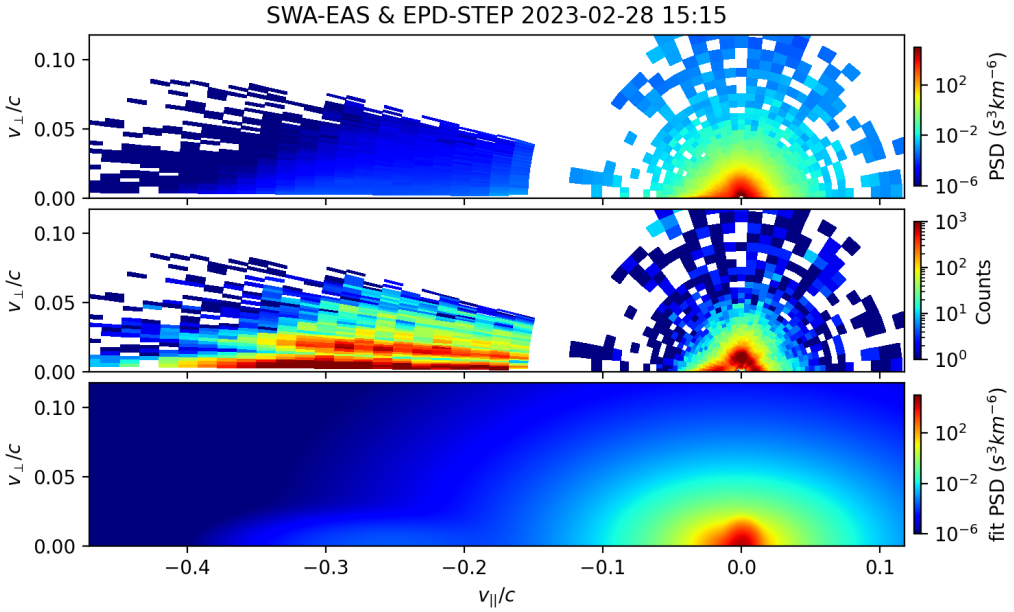

Figure 4.2: ALPS interpolated SWA-EAS data and a fit of the distribution.

4.2.3 Stability of the velocity distribution

Using out fit parameters, we can generate a regular $(p_\parallel, p_\perp)$ grid. We call this table an `f0-table` and it can be used for runnuing the ALPS dispersion relation solver. For an introduction into working with ALPS, see appendix A.

Numerically solving the hot plasma dispersion relation reveals that the observed VDF is stable. In figure 4.3, we show the growth rate γ as a function of $k\lambda_D$ for the observed VDF and for modified VDFs with lower parallel temperatures of the beam.

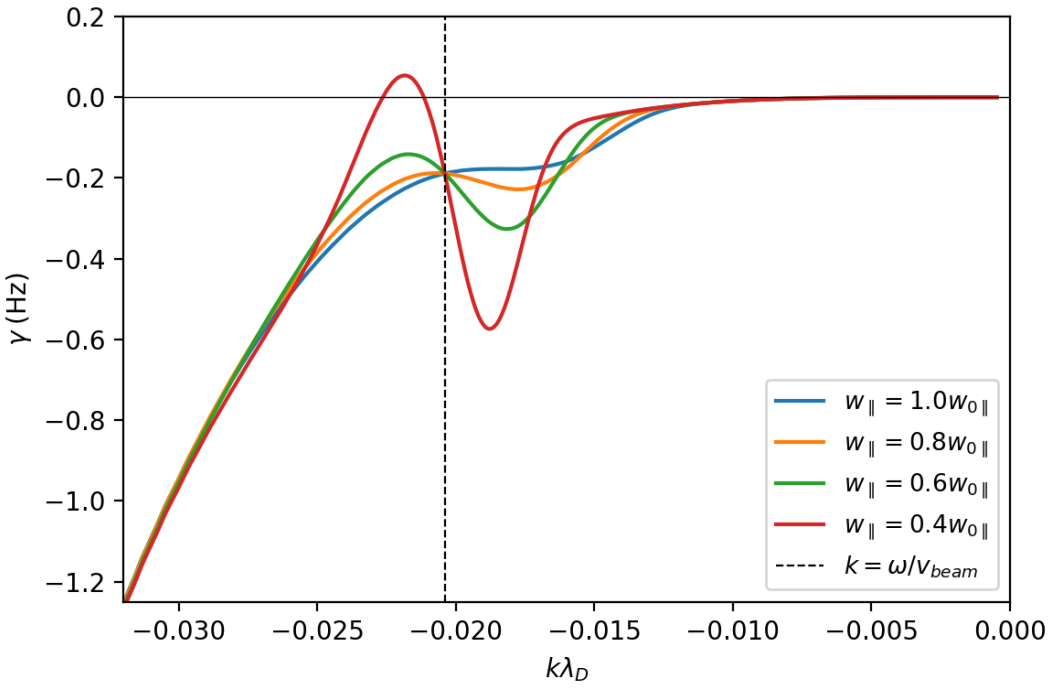

Figure 4.3: The growth rate of Langmuir waves γ obtained by running the ALPS dispersion relation solver on the model electron VDFs. The blue line corresponds to the observed VDF parameters with a plateau. The other solutions correspond to a modified VDF which has a lower parallel beam thermal velocity w.

Due to technical limitations the interaction occurs too quickly for the unmodified population to be observed by the electron instruments. Additionally, the interaction is occurring all the way along the beams path, so the deviations from the observed plateau distributions are relatively small.

Decreasing the beam temperature allows us to estimate how the beam looked like before an interaction with the background plasma occurred. The lower parallel beam temperature causes a higher phase space density around the beam drift velocity, while perserving the total number density of the beam population.

We show the reduced VDFs for observed and modified temperatures in figure 4.4. We see that for the unstable configuration $w_\parallel = w_{0\parallel}$, there is a second hump in the reduced VDF. The stability of the remaining single humped reduced VDFs is in agreement with Gardners theorem [Gardner, 1963][Gurnett and Bhattacharjee, 2017, chapter 9.5].

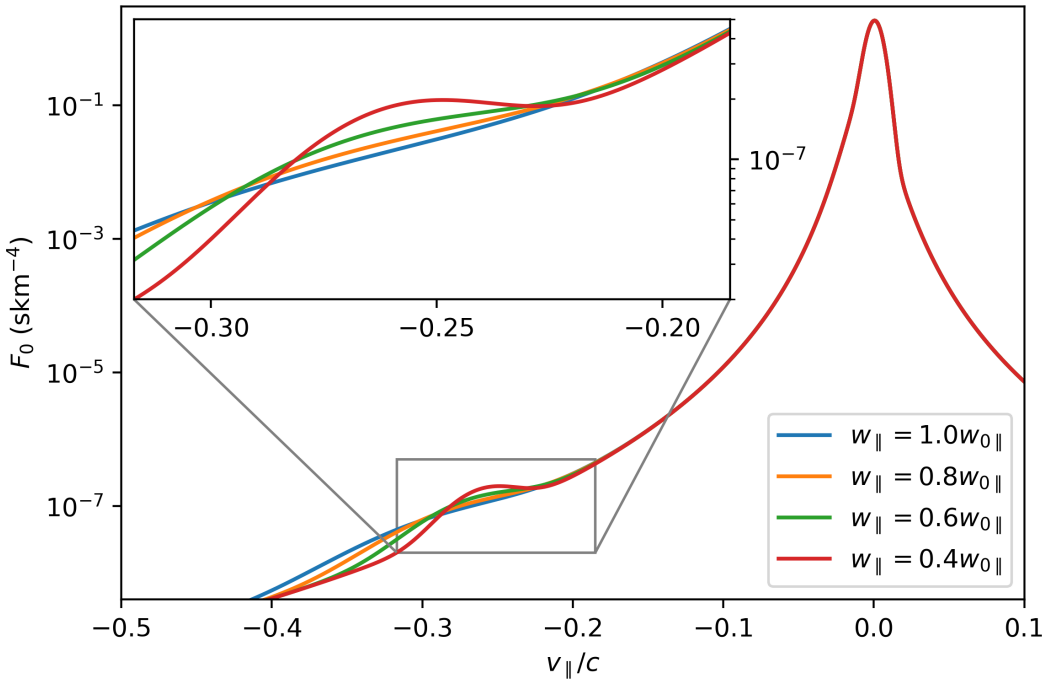

Figure 4.4: The reduced VDF for the fitted model parameters and for a modified beam parallel temperature.

With a simple thought experiment we can show that plasma density inhomogeneities provide another possibility for an environment prone to the instability. Let us consider an electron beam entering a region with a lower plasma density. The core population provides a lower contribution to the total VDF, and the same electron beam now has a higher chance at producing a positive gradient in the reduced velocity distribution function.

This positive gradient in the reduced VDF can cause the growth of Langmuir waves, analogously to the process of Landau damping which stops Langmuir waves from propagating freely in space. However, if we consider an inverse situation where an electron beam enters a denser environment, the waves become more dampened due to the Landau damping from the core population.

5. Analysis of observed waves

5.1 Event overview

In this chapter we investigate the wave observations in the source regions of type III solar radio emissions. We will focus on the observations from 28th February 2023 recorded by the Solar Orbiter spacecraft. The magnetic field orientation during during these observations provide a unique opportunity to study the wave polarization.

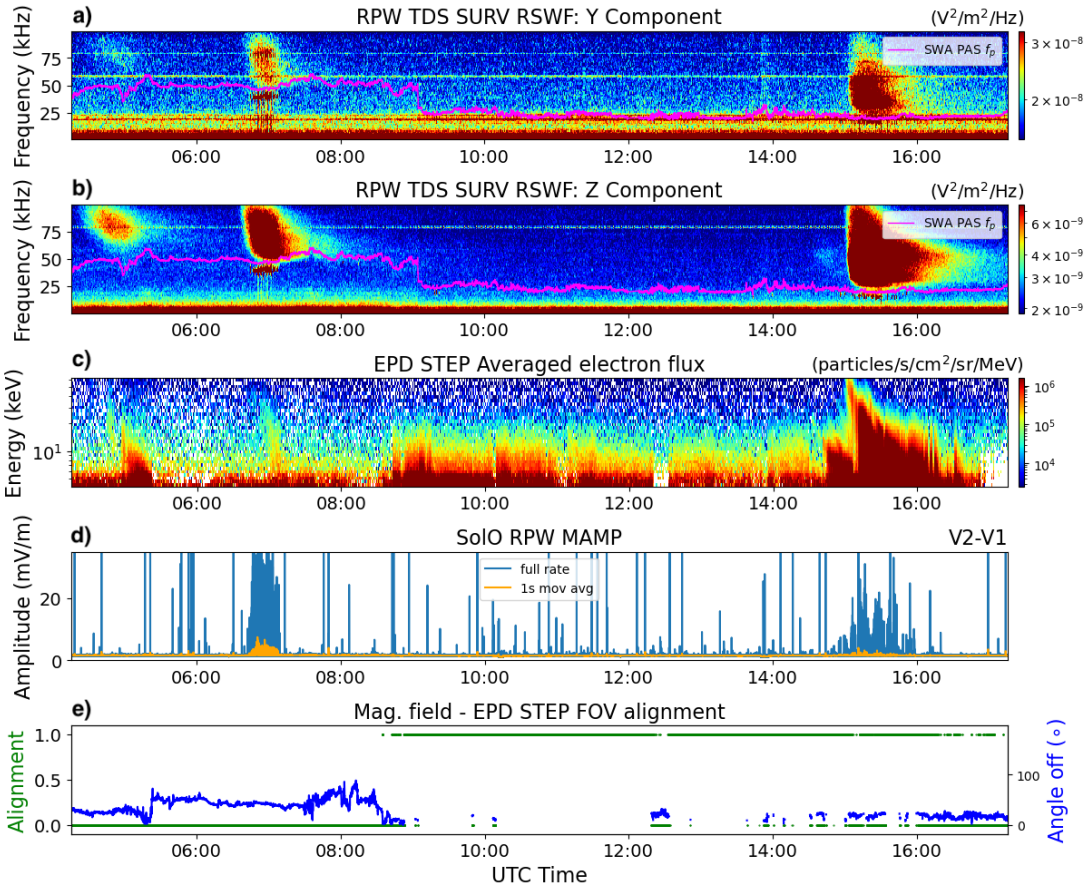

Figure 5.1: Overview of in situ observations from the Solar Orbiter spacecraft on the 28th February 2023. Panels a) and b) show the RPW-TDS time-frequency spectrogram of the SRF Y and Z components respectively, panel c) shows the EPD-STEP electron data, panel d) shows the RPW-TDS continuously sampled maximum amplitude data and panel e) shows the binary magnetic field alignment with the EPD-STEP field of view and the angle between the magnetic field and the edge of the EPD-STEP field when the magnetic field is outside the field of view.

On this day, several in situ type III radio emissions were observed by the Solar Orbiter. In figure 5.1 we show an overview of the in situ measurements, showing the three radio emissions occurring at ∼04:20, ∼06:40 and ∼15:05 UTC.

During the second event at ∼06:40 the SBM2 mode (described in section 3) was triggered, allowing for 192 snapshots of Langmuir waves to be recorded. During this time, the magnetic field was nearly aligned with the Y-Z plane in the SRF reference frame. For this reason the magnetic field is outside the EPD-STEP field of view and the beam observation only shows the edge of the electron beam.

Although the magnetic field orientation limits our direct electron observation capabilities during this event, we still see the edge of the electron beam, which is dispersed in velocity space.

5.2 Waveform polarization

The magnetic field vector $\mathbf{B}$ orientation near the Y-Z plane provides an advantage when analyzing the polarization of the recorded waveform signal. To perform this analysis with 3D measurements we would convert the waveform data to field aligned coordinates. Since the electric waveform signal $\mathbf{E}_{YZ}$ is recorded only in the 2D Y-Z plane, we must project the magnetic field on the Y-Z plane $\mathbf{B}_{YZ}$. Then, we can estimate the parallel component of the electric field.

If we assumed purely longitudinal waves ($E_\perp = 0$), the parallel component could be estimated as

$$E_{||} = \frac{\mathbf{E}_{YZ} \cdot \hat{\mathbf{B}}_{YZ}}{cos(\theta)}, \tag{5.1}$$

where θ is the angle between the magnetic field vector $\mathbf{B}$ and the Y-Z plane. This gives us a good estimate if there are purely electrostatic Langmuir waves present.

In order to account for the Z-mode waves, we will instead assume that $E_X = 0$ and estimate the parallel component as

$$E_{\|} = \mathbf{E}_{YZ} \cdot \hat{\mathbf{B}}_{YZ}. \tag{5.2}$$

Under the same assumption, we estimate the perpendicular component as

$$E_\perp = \mathbf{E}_{YZ} \cdot \begin{bmatrix} \hat{B}_{YZ,2} \\ -\hat{B}_{YZ,1} \end{bmatrix}. \tag{5.3}$$

Having approximately estimated the transformation of the electric field data into field aligned coordinates, we can focus on analyzing the individual components. To analyze signals at one characteristic frequency a particularly useful tool is the Hilbert transform. It allows us to get the instantaneous phase of the signal. The result of performing the Hilbert transform on the estimates of parallel and perpendicular components is shown in figure 5.2.

This analysis allows us to study the relative phase, of the two components. From the first plot in figure 5.2, we can see that the relative phase is very noisy when no waves are observed and when wave growth occurs the relative phase between the two components is shifting. We can also see both linear and elliptical polarization as demonstrated by the hodograms in figure 5.2.

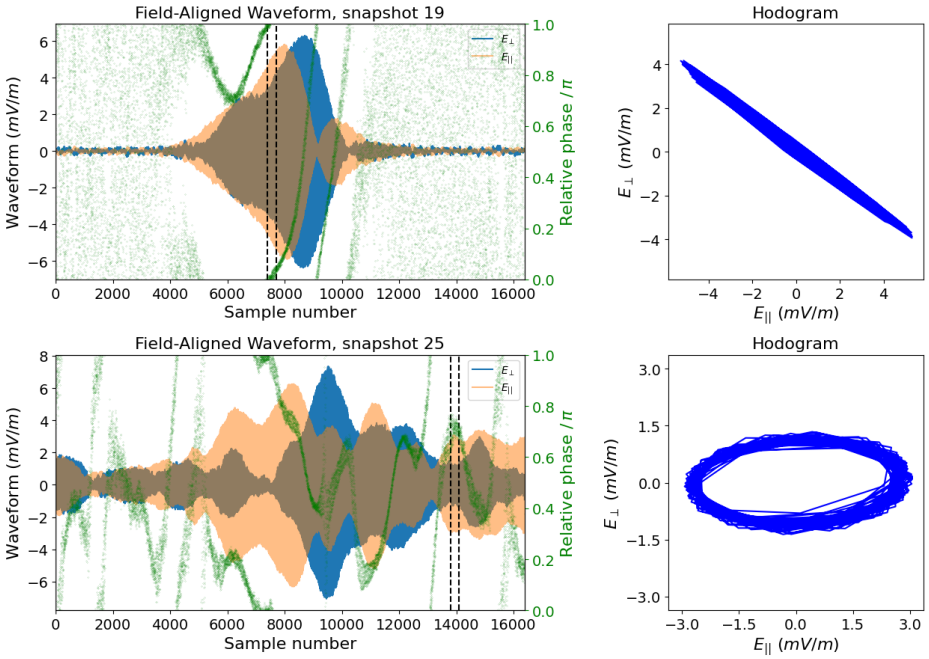

Figure 5.2: The field aligned electric field waveform data and their Hilbert transform relative phase shift is shown on the left. The plots on the right show the hodogram of the electric field using the snapshots between the dashed vertical lines.

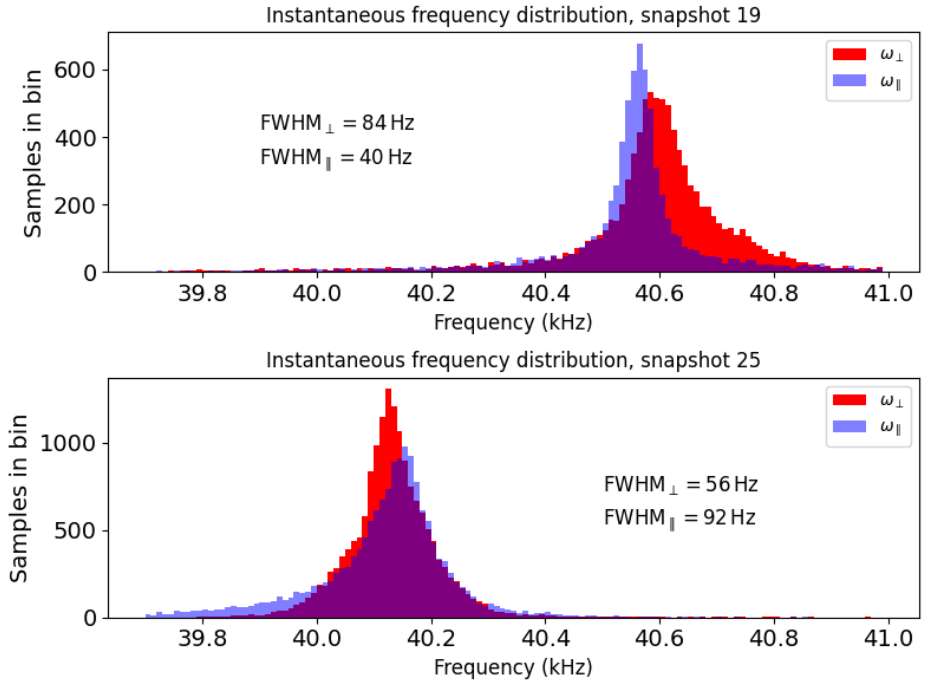

Figure 5.3: The instantaneous frequency distributions for the field aligned components of the electric field waveforms.

The linearly polarized field aligned oscillations could be explained by Langmuir waves or beam mode waves. However there are certainly more wave modes at play. This can be shown by further analyzing the signal. We can study the

instantaneous frequency spectrum of the two components, as shown in figure 5.3. The width of the instantaneous frequency distribution for the parallel and perpendicular components are different and shifted in frequency.

By analyzing all of the 192 snapshots recorded we have found that the parallel frequency distribution is usually wider than for the perpendicular component. These different widths of the frequency distribution could be explained by the presence of multiple wave modes.

Conclusion

In chapter 1, we introduced the fluid approach in order to explain the shape of the Sun's magnetic field. Then we delved into the kinetic plasma theory, briefly expressing the cold plasma dispersion relation and deriving the dispersion relation for hot plasma.

To provide an overview of the type III radio emissions, we summarized the current theoretical understanding of these events in chapter (2). We discussed the various shapes of velocity distribution functions (VDF)s and how they can be modeled.

The multiple populations which the solar wind consists of were also introduced, allowing us to discuss their contributions to the Langmuir instability. We discussed the available wave modes in the solar wind and provided an intuitive description of Landau damping.

An introduction to the Solar Orbiter spacecraft and its instruments was provided in chapter 3.

In chapter 4, we have described the principle of Langmuir wave generation in the source regions of type III radio emissions by using observational electron velocity distribution data. We were able to describe the studied system by a model and determine the stability of the observed electron VDF.

We developed a fitting procedure which considers the Poisson distribution of the observational data. This method was then used to obtain a model of the velocity distribution. This allowed us to numerically solve the hot plasma dispersion using the ALPS solver.

Since the instability process quickly causes the velocity distribution function to become stable again, we cannot directly observe an unstable configuration. This was confirmed by the dispersion relation obtained from ALPS. However, we can model the unmodified beam population only by changing its temperature. This is sufficient to cause the Langmuir instability at parameters close to the actually observed electron distribution.

A detailed analysis of the generated Langmuir waves is presented in chapter 5. By performing the Hilbert transform analysis of observed electric field waveforms, we show the presence of multiple wave modes.

The frequency distributions of parallel and perpendicular electric field components suggest the presence of multiple wave modes.

By performing a Hilbert transform analysis of the measured waveform signal we show how the wave polarization drifts in time. This indicates that the signal consists of a range of frequencies.

Bibliography

H. Alfvén. Existence of electromagnetic-hydrodynamic waves. *Nature*, 150(3805): 405–406, Oct 1942. ISSN 1476-4687. doi: 10.1038/150405d0. URL https://doi.org/10.1038/150405d0.

L. Biermann. Kometenschweife und solare Korpuskularstrahlung. , 29:274, January 1951. doi: 10.1007/BF00150860. URL https://doi.org/10.1007/BF00150860.

M. Y. Boudjada, A. Abou el Fadl, P. H. M. Galopeau, E. Al-Haddad, and H. Lammer. Observations of solar type iii radio bursts by cassini/rpws experiment. *Advances in Radio Science*, 18:83–87, 2020. doi: 10.5194/ars-18-83-2020. URL https://ars.copernicus.org/articles/18/83/2020/.

F. F. Chen. *Introduction to Plasma Physics and Controlled Fusion, Vol. 1: Plasma Physics*. Plenum Press, New York, 1984. ISBN 0-306-41332-9. doi: 10.1007/978-3-319-22309-4.

ESA/ATG MediaLab. Solar Orbiter, Oct 2019. URL https://www.esa.int/ESA_Multimedia/Images/2019/10/Solar_Orbiter11.

C. S. Gardner. Comment on "Stability of Step Shocks". *The Physics of Fluids*, 6(9):1366–1367, 09 1963. ISSN 0031-9171. doi: 10.1063/1.1706917. URL https://doi.org/10.1063/1.1706917.

S. P. Gary. *Theory of Space Plasma Microinstabilities*. Cambridge Univesity Press, 1993. ISBN 0-521-43167-0.

D. A. Gurnett and R. R. Anderson. Electron plasma oscillations associated with type iii radio bursts. *Science*, 194(4270):1159–1162, 1976. doi: 10.1126/science.194.4270.1159. URL https://www.science.org/doi/abs/10.1126/science.194.4270.1159.

D. A. Gurnett and A. Bhattacharjee. *Introduction to Plasma Physics: With Space, Laboratory and Astrophysical Applications*. Cambridge University Press, 2 edition, 2017. doi: 10.1017/9781139226059.

D. A. Gurnett and L. A. Frank. Electron plasma oscillations associated with type iii radio emissions and solar electrons. *Solar Physics*, 45(2):477–493, Dec 1975. ISSN 1573-093X. doi: 10.1007/BF00158464. URL https://doi.org/10.1007/BF00158464.

T. S. Horbury, H. O'Brien, I. Carrasco Blazquez, M. Bendyk, P. Brown, R. Hudson, V. Evans, T. M. Oddy, C. M. Carr, T. J. Beek, E. Cupido, S. Bhattacharya, J. A. Dominguez, L. Matthews, V. R. Myklebust, B. Whiteside, S. D. Bale, W. Baumjohann, D. Burgess, V. Carbone, P. Cargill, J. Eastwood, G. Erdös, L. Fletcher, R. Forsyth, J. Giacalone, K. H. Glassmeier, M. L. Goldstein, T. Hoeksema, M. Lockwood, W. Magnes, M. Maksimovic, E. Marsch, W. H. Matthaeus, N. Murphy, V. M. Nakariakov, C. J. Owen, M. Owens,

J. Rodriguez-Pacheco, I. Richter, P. Riley, C. T. Russell, S. Schwartz, R. Vainio, M. Velli, S. Vennerstrom, R. Walsh, R. F. Wimmer-Schweingruber, G. Zank, D. Müller, I. Zouganelis, and A. P. Walsh. The Solar Orbiter magnetometer. , 642:A9, October 2020. doi: 10.1051/0004-6361/201937257. URL https://www.aanda.org/articles/aa/pdf/2020/10/aa37257-19.pdf.

I. C. Jebaraj, V. Krasnoselskikh, M. Pulupa, J. Magdalenic, and S. D. Bale. Fundamental–harmonic pairs of interplanetary type iii radio bursts. *The Astrophysical Journal Letters*, 955(1):L20, sep 2023. doi: 10.3847/2041-8213/acf857. URL https://dx.doi.org/10.3847/2041-8213/acf857.

K. G. Klein, D. Verscharen, T. Koskela, and D. Stansby. danielver02/alps: Zenodo release, June 2023. URL https://doi.org/10.5281/zenodo.8075682.

E. P. Kontar and H. A. S. Reid. Onsets and spectra of impulsive solar energetic electron events observed near the earth. *The Astrophysical Journal*, 695(2): L140, mar 2009. doi: 10.1088/0004-637X/695/2/L140. URL https://dx.doi.org/10.1088/0004-637X/695/2/L140.

V. Krupar, M. Maksimovic, E. P. Kontar, A. Zaslavsky, O. Santolik, J. Soucek, O. Kruparova, J. P. Eastwood, and A. Szabo. Interplanetary type iii bursts and electron density fluctuations in the solar wind. *The Astrophysical Journal*, 857(2):82, apr 2018. doi: 10.3847/1538-4357/aab60f. URL https://dx.doi.org/10.3847/1538-4357/aab60f.

G. Livadiotis and D. J. McComas. Understanding kappa distributions: A toolbox for space science and astrophysics. *Space Science Reviews*, 175(1):183–214, Jun 2013. ISSN 1572-9672. doi: 10.1007/s11214-013-9982-9. URL https://doi.org/10.1007/s11214-013-9982-9.

C. Y. Lorfing and H. A. S. Reid. Solar electron beam velocities that grow langmuir waves in the inner heliosphere. *Solar Physics*, 298(4):52, Apr 2023. ISSN 1573-093X. doi: 10.1007/s11207-023-02145-2. URL https://doi.org/10.1007/s11207-023-02145-2.

C. Y. Lorfing, H. A. S. Reid, R. Gómez-Herrero, M. Maksimovic, G. Nicolaou, C. J. Owen, J. Rodriguez-Pacheco, D. F. Ryan, D. Trotta, and D. Verscharen. Solar electron beam—langmuir wave interactions and how they modify solar electron beam spectra: Solar orbiter observations of a match made in the heliosphere. *The Astrophysical Journal*, 959(2):128, dec 2023. doi: 10.3847/1538-4357/ad0be3. URL https://dx.doi.org/10.3847/1538-4357/ad0be3.

M. Maksimovic, V. Pierrard, and P. Riley. Ulysses electron distributions fitted with kappa functions. *Geophysical Research Letters*, 24(9):1151–1154, 1997. doi: https://doi.org/10.1029/97GL00992. URL https://agupubs.onlinelibrary.wiley.com/doi/abs/10.1029/97GL00992.

M. Maksimovic, S. D. Bale, T. Chust, Y. Khotyaintsev, V. Krasnoselskikh, M. Kretzschmar, D. Plettemeier, H. O. Rucker, J. Souček, M. Steller, Š. Štverák, P. Trávníček, A. Vaivads, S. Chaintreuil, M. Dekkali, O. Alexandrova, P.-A. Astier, G. Barbary, D. Bérard, X. Bonnin, K. Boughedada, B. Cecconi, F. Chapron, M. Chariet, C. Collin, Y. de Conchy, D. Dias, L. Guéguen,

L. Lamy, V. Leray, S. Lion, L. R. Malac-Allain, L. Matteini, Q. N. Nguyen, F. Pantellini, J. Parisot, P. Plasson, S. Thijs, A. Vecchio, I. Fratter, E. Bellouard, E. Lorfèvre, P. Danto, S. Julien, E. Guilhem, C. Fiachetti, J. Sanisidro, C. Laffaye, F. Gonzalez, B. Pontet, N. Quéruel, G. Jannet, P. Fergeau, J.-Y. Brochot, G. Cassam-Chenai, T. Dudok de Wit, M. Timofeeva, T. Vincent, C. Agrapart, G. T. Delory, P. Turin, A. Jeandet, P. Leroy, J.-C. Pellion, V. Bouzid, B. Katra, R. Piberne, W. Recart, O. Santolík, I. Kolmašová, V. Krupař, O. Krupařová, D. Píša, L. Uhlíř, R. Lán, J. Baše, L. Ahlèn, M. André, L. Bylander, V. Cripps, C. Cully, A. Eriksson, S.-E. Jansson, E. P. G. Johansson, T. Karlsson, W. Puccio, J. Břínek, H. Öttacher, M. Panchenko, M. Berthomier, K. Goetz, P. Hellinger, T. S. Horbury, K. Issautier, E. Kontar, S. Krucker, O. Le Contel, P. Louarn, M. Martinović, C. J. Owen, A. Retino, J. Rodríguez-Pacheco, F. Sahraoui, R. F. Wimmer-Schweingruber, A. Zaslavsky, and I. Zouganelis. The solar orbiter radio and plasma waves (rpw) instrument. *AA*, 642:A12, 2020. doi: 10.1051/0004-6361/201936214. URL `https://doi.org/10.1051/0004-6361/201936214`.

D. B. Melrose. The Emission Mechanisms for Solar Radio Bursts. , 26(1):3–38, May 1980. doi: 10.1007/BF00212597.

R. Müller-Mellin, S. Böttcher, J. Falenski, E. Rode, L. Duvet, T. Sanderson, B. Butler, B. Johlander, and H. Smit. The solar electron and proton telescope for the stereo mission. *Space Science Reviews*, 136(1):363–389, Apr 2008. ISSN 1572-9672. doi: 10.1007/s11214-007-9204-4. URL `https://doi.org/10.1007/s11214-007-9204-4`.

C. J. Owen, R. Bruno, S. Livi, P. Louarn, K. Al Janabi, F. Allegrini, C. Amoros, R. Baruah, A. Barthe, M. Berthomier, S. Bordon, C. Brockley-Blatt, C. Brysbaert, G. Capuano, M. Collier, R. DeMarco, A. Fedorov, J. Ford, V. Fortunato, I. Fratter, A. B. Galvin, B. Hancock, D. Heirtzler, D. Kataria, L. Kistler, S. T. Lepri, G. Lewis, C. Loeffler, W. Marty, R. Mathon, A. Mayall, G. Mele, K. Ogasawara, M. Orlandi, A. Pacros, E. Penou, S. Persyn, M. Petiot, M. Phillips, L. Přech, J. M. Raines, M. Reden, A. P. Rouillard, A. Rousseau, J. Rubiella, H. Seran, A. Spencer, J. W. Thomas, J. Trevino, D. Verscharen, P. Wurz, A. Alapide, L. Amoruso, N. André, C. Anekallu, V. Arciuli, K. L. Arnett, R. Ascolese, C. Bancroft, P. Bland, M. Brysch, R. Calvanese, M. Castronuovo, I. Čermák, D. Chornay, S. Clemens, J. Coker, G. Collinson, R. D'Amicis, I. Dandouras, R. Darnley, D. Davies, G. Davison, A. De Los Santos, P. Devoto, G. Dirks, E. Edlund, A. Fazakerley, M. Ferris, C. Frost, G. Fruit, C. Garat, V. Génot, W. Gibson, J. A. Gilbert, V. de Giosa, S. Gradone, M. Hailey, T. S. Horbury, T. Hunt, C. Jacquey, M. Johnson, B. Lavraud, A. Lawrenson, F. Leblanc, W. Lockhart, M. Maksimovic, A. Malpus, F. Marcucci, C. Mazelle, F. Monti, S. Myers, T. Nguyen, J. Rodriguez-Pacheco, I. Phillips, M. Popecki, K. Rees, S. A. Rogacki, K. Ruane, D. Rust, M. Salatti, J. A. Sauvaud, M. O. Stakhiv, J. Stange, T. Stubbs, T. Taylor, J.-D. Techer, G. Terrier, R. Thibodeaux, C. Urdiales, A. Varsani, A. P. Walsh, G. Watson, P. Wheeler, G. Willis, R. F. Wimmer-Schweingruber, B. Winter, J. Yardley, and I. Zouganelis. The solar orbiter solar wind analyser

(swa) suite. *AA*, 642:A16, 2020. doi: 10.1051/0004-6361/201937259. URL https://doi.org/10.1051/0004-6361/201937259.

E. N. Parker. Dynamics of the Interplanetary Gas and Magnetic Fields. , 128: 664, November 1958. doi: 10.1086/146579.

H. Reid, S. Andrew, and H. Ratcliffe. A review of solar type iii radio bursts. *Research in Astronomy and Astrophysics*, 14(7):773, jul 2014. doi: 10.1088/1674-4527/14/7/003. URL https://dx.doi.org/10.1088/1674-4527/14/7/003.

H. A. S. Reid and E. P. Kontar. Evolution of the solar flare energetic electrons in the inhomogeneous inner heliosphere. *Solar Physics*, 285(1–2):217–232, June 2012. ISSN 1573-093X. doi: 10.1007/s11207-012-0013-x. URL http://dx.doi.org/10.1007/s11207-012-0013-x.

P. A. Robinson, I. H. Cairns, and D. A. Gurnett. Connection between Ambient Density Fluctuations and Clumpy Langmuir Waves in Type III Radio Sources. , 387:L101, March 1992. doi: 10.1086/186315.

J. Rodríguez-Pacheco, R. F. Wimmer-Schweingruber, G. M. Mason, G. C. Ho, S. Sánchez-Prieto, M. Prieto, C. Martín, H. Seifert, G. B. Andrews, S. R. Kulkarni, L. Panitzsch, S. Boden, S. I. Böttcher, I. Cernuda, R. Elftmann, F. Espinosa Lara, R. Gómez-Herrero, C. Terasa, J. Almena, S. Begley, E. Böhm, J. J. Blanco, W. Boogaerts, A. Carrasco, R. Castillo, A. da Silva Fariña, V. de Manuel González, C. Drews, A. R. Dupont, S. Eldrum, C. Gordillo, O. Gutiérrez, D. K. Haggerty, J. R. Hayes, B. Heber, M. E. Hill, M. Jüngling, S. Kerem, V. Knierim, J. Köhler, S. Kolbe, A. Kulemzin, D. Lario, W. J. Lees, S. Liang, A. Martínez Hellín, D. Meziat, A. Montalvo, K. S. Nelson, P. Parra, R. Paspirgilis, A. Ravanbakhsh, M. Richards, O. Rodríguez-Polo, A. Russu, I. Sánchez, C. E. Schlemm, B. Schuster, L. Seimetz, J. Steinhagen, J. Tammen, K. Tyagi, T. Varela, M. Yedla, J. Yu, N. Agueda, A. Aran, T. S. Horbury, B. Klecker, K.-L. Klein, E. Kontar, S. Krucker, M. Maksimovic, O. Malandraki, C. J. Owen, D. Pacheco, B. Sanahuja, R. Vainio, J. J. Connell, S. Dalla, W. Dröge, O. Gevin, N. Gopalswamy, Y. Y. Kartavykh, K. Kudela, O. Limousin, P. Makela, G. Mann, H. Önel, A. Posner, J. M. Ryan, J. Soucek, S. Hofmeister, N. Vilmer, A. P. Walsh, L. Wang, M. E. Wiedenbeck, K. Wirth, and Q. Zong. The energetic particle detector - energetic particle instrument suite for the solar orbiter mission. *AA*, 642:A7, 2020. doi: 10.1051/0004-6361/201935287. URL https://doi.org/10.1051/0004-6361/201935287.

K. Roennmark. Waves in homogeneous, anisotropic multicomponent plasmas (WHAMP), June 1982.

Ondrej Santolik. *Studium rozdelovaci funkce plasmatu a vlnove rozdelovaci funkce v kosmickem prostoru (in czech).* Phd thesis, Charles University, Praha, Czechia, October 1995.

T. H. Stix. *Waves in Plasmas.* American Inst. of Physics, 1992. ISBN 9780883188590. URL https://books.google.co.uk/books?id=OsOWJ8iHpmMC.

B. T. Tsurutani, G. P. Zank, V. J. Sterken, K. Shibata, T. Nagai, A. J. Mannucci, D. M. Malaspina, G. S. Lakhina, S. G. Kanekal, K. Hosokawa, R. B. Horne, R. Hajra, K. Glassmeier, C. T. Gaunt, P. Chen, and S. Akasofu. Space plasma physics: A review. *IEEE Transactions on Plasma Science*, 51(7):1595–1655, 2023. doi: 10.1109/TPS.2022.3208906.

D. Verscharen, K. G. Klein, B. D. G. Chandran, M. L. Stevens, C. S. Salem, and S. D. Bale. Alps: the arbitrary linear plasma solver. *Journal of Plasma Physics*, 84(4):905840403, 2018. doi: 10.1017/S0022377818000739. URL `https://doi.org/10.1017/S0022377818000739`.

D. Verscharen, B. D. G. Chandran, E. Boella, J. Halekas, M. E. Innocenti, V. K. Jagarlamudi, A. Micera, V. Pierrard, Š. Štverák, I. Y. Vasko, M. Velli, and P. L. Whittlesey. Electron-driven instabilities in the solar wind. *Frontiers in Astronomy and Space Sciences*, 9, 2022. ISSN 2296-987X. doi: 10.3389/fspas.2022.951628. URL `https://www.frontiersin.org/articles/10.3389/fspas.2022.951628`.

J. P. Wild. Observations of the spectrum of high-intensity solar radiation at metre wavelengths. iii. isolated bursts. *Australian Journal of Chemistry*, 3(4):541–557, 1950. doi: 10.1071/CH9500541. URL `https://doi.org/10.1071/CH9500541`.

V. V. Zheleznyakov and V. V. Zaitsev. The Theory of Type III Solar Radio Bursts. II. , 14:250, October 1970.

Š. Štverák, M. Maksimovic, P. M. Trávníček, E. Marsch, A. N. Fazakerley, and E. E. Scime. Radial evolution of nonthermal electron populations in the low-latitude solar wind: Helios, cluster, and ulysses observations. *Journal of Geophysical Research: Space Physics*, 114(A5), 2009. doi: https://doi.org/10.1029/2008JA013883. URL `https://agupubs.onlinelibrary.wiley.com/doi/abs/10.1029/2008JA013883`.

List of Figures

List of Tables

List of Abbreviations

Acronyms

ALPS The Arbitrary Linear Plasma Solver. 16, 27, 28, 31, 32, 38, 44, 45, 47–51

CME Coronal mass ejection. 17

EAS Electron Analyser System. 24, 25, 28, 29, 31, 44

EPD Energetic Particle Detector. 22, 25, 28, 34, 35, 44

EPT Electron Proton Telescope. 25, 26

IMP Interplanetary Monitoring Platform. 21

ISEE International Sun Earth Explore. 21

MAG Magnetometer. 22, 26

MAMP Maximum amplitude data product. 23, 24

MHD Magnetohydrodynamics. 4, 6, 7, 11

RPW Radio and Plasma Waves. 22, 23, 34

RSWF Regular snapshot waveform data product. 23

SBM Selected Burst Mode. 24, 35

SRF Spacecraft Reference Frame. 22, 23, 29, 34, 35, 44

STEP SupraThermal Electron Proton sensor. 25, 28, 29, 34, 35, 44

STEREO Solar TErrestrial RElations Observatory. 21

STEREO/SEPT Solar TErrestrial RElations Observatory and its Solar Electron Proton Telescope (SEPT) Experiment. 25

SWA Solar Wind Analyzer. 22, 24, 28, 31, 44

TDS Time Domain Sampler. 23, 24, 34

TSWF Triggered snapshot waveform data product. 23

VDF Velocity distribution function. 17–20, 28, 29, 31–33, 38, 44

WHAMP Waves in homogeneous, anisotropic multicomponent plasmas. 44, 47, 48, 51

A. ALPS in electron mode

Numerical plasma dispersion relation solvers such as ALPS [Klein et al., 2023] or WHAMP [Roennmark, 1982] use normalized physical quantities to simplify the underlying calculations. The normalization converts physical parameters such as temperature or velocity to dimensionless quantities and these converted parameters can then be used to run the dispersion relation solver.

By default, ALPS uses the proton normalization. This normalization, described by Verscharen et al. [2018], is used in the example test files available on the ALPS github page. However, using the proton normalization for electron kinetic instabilities can result in lower numerical precision, since these instabilities typically occur at high frequencies compared to the proton cyclotron frequency.

A.1 Normalization

For achieving better numerical precision and better usability, we use ALPS in electron mode. This means using a non-standard normalization which we describe here.

A.1.1 General description

For each species ALPS requires a well defined distribution function f_{0s}. The required format is a regular rectangular momentum grid (parallel and perpendicular momentum), stored in a distribution function table (`.array` file). When running ALPS, the input file contains the name of the corresponding `f0-table`s, as well as other parameters which describe the plasma. The normalization ALPS uses is explained by table A.1, containing formulae for performing the normalization.

Variable	symbol	Physical units	ALPS normalized
Electron mass	m_e	$9.109 \cdot 10^{-31}\,\mathrm{kg}$	1
Electron charge	q_e	$-1.602 \cdot 10^{-19}\,\mathrm{C}$	$+1$
Proton charge	q_p	$1.602 \cdot 10^{-19}\,\mathrm{C}$	-1
Electron gyrofrequency	Ω_e	$\frac{qB}{m_e}$	1
Modified Alfvén speed	v_A, `vA`	$\frac{B}{\sqrt{\mu_0 n m_e}}$	v_A/c
Electron skin depth	d_p	$\frac{v_A}{\Omega_e}$	1
Momentum of species	p_s, `ps`	$v_s m_s$	$\frac{p_s}{v_A m_e}$

Table A.1: Constants and formulas useful for determining the input parameters for ALPS in electron mode.

Additionally, it is useful to list a few more parameters which are used to describe the plasma in ALPS. The temperature of the plasma is determined by

the plasma beta parameter

$$\beta = \frac{nk_BT}{B^2/2\mu_0}. \tag{A.1}$$

This parameter also depends on the magnetic field, however the magnetic field is already fixed by setting the electron gyrofrequency (cyclotron frequency).

A.1.2 Example case

In this thesis we used the ALPS dispersion relation solver for modeling electron kinetic instabilities caused by an electron beam. To test the validity of our results, we will compare the results of the ALPS solver with the WHAMP solver.

In this exercise we focus on a simple case with three Maxwellian populations consisting of the electron core, electron beam and proton background. The temperatures of these three populations are equal and the number density ratio of the electron beam to the background proton distribution is $n_b/n_p = 0.001$. Two cases are studied, where the electron beam velocity v_b is set in multiples of the thermal speed $w = \sqrt{\frac{2k_BT_e}{m_e}}$. This problem was adapted from [Gary, 1993, sec. 3.2.2] who solves it for the 1D case.

We will study the cases $v_b = 5w$ and $v_b = 10w$, which should produce the Langmuir instability and the beam mode instability respectively. Our physical parameters for both cases are listed in table A.2.

When determining the ALPS normalized parameters, it is convenient to realize the equivalence of the three parameters B, n, T and Ω_e, β, v_A. It is an easy exercise to show that from one set we can obtain the other using formulas from table A.1 and equation (A.1).

B (nT)	n (cm^{-3})	T (K)	E_b (eV)	v_A (km/s)	v_b (km/s)	v_p (km/s)
15	25	140000	302	2804	10300	10.3
15	25	140000	1206	2804	20600	20.6

Π_e (kHz)	Ω_e (Hz)	k_{res} (m^{-1})	d_p (m)	β	λ_D (m)
44.9	420	1063	0.0274	0.540	5.16
44.9	420	1063	0.0137	0.540	5.16

Table A.2: Plasma parameters used for generating the ALPS inputs.

Note that to satisfy the zero-current condition, in table A.2, we calculated the necessary drift velocity of the background protons v_p. These drift velocities are relative to the stationary electron core population. Having the background electron distribution with zero drift velocity will be convenient for running ALPS, since the first population is required to have a zero drift velocity.

A.2 Generating f0-tables

To generate the velocity distributions, it is advised to start with a test file available at the ALPS github page and modify it as needed.

The electron mode requires a different approach for setting up the species. (Different than the usual proton normalization.) The used configuration of the species is described in table A.3.

	Description	Motion	Charge	Mass	Density
1	Electron background	stationary	1	1	1
2	Electron beam	moving	1	1	n_b/n_e
3	Proton background	moving (zero current)	-1	1836	n_p/n_e

Table A.3: List of the ALPS species for modeling an electron beam interacting with the background electron VDF

Using the formulae from table A.1 we can calculate parameters, which are required in the `*_dist.in` file. Running the `generate_distribution` script then uses this file as input for producing the `f0-tables`. Some of the parameters (such as the relative density) are not used during the `f0-table` generation. However, they will be useful for creating the input files for running ALPS. We list all of the ALPS normalized parameters for $v_b = 5w$ and $v_b = 10w$ in table A.4. We note that the number densities are again normalized to species 1 (the electron background distribution).

It is easy to verify that the parameters in table A.4 satisfy the zero current condition

$$\sum_s n_s q_s v_s = 0 \tag{A.2}$$

as well as the quasineutrality condition

$$\sum_s n_s q_s = 0. \tag{A.3}$$

If these conditions were not met, some current driven instabilities may appear in our solution of the dispersion relation.

After we have determined all the necessary parameters we can modify the `example_dist.in` file in the `distribution` directory and run the command `./generate_distribution example_dist.in` to generate the `f0-table`s. This command also outputs the ideal fit parameters for the distribution, which should be copied to the ALPS input file before running it. This is because ALPS uses the fit to perform hybrid analytic continuation, for more detail see [Verscharen et al., 2018, section 3.2].

	ALPS variable name	$v_b = 5w$	$v_b = 10w$
Global params	`nspec`	3	3
	`beta`, `bM_betas`	0.53977	0.53977
	`vA` (v_A/c)	0.00935	0.00935
Species 1	`ms_read`, `mm`	1	1
	`ps`	0	0
	`nn`	1	1
	`qq`	1	1
	`taus`	1	1
Species 2	`ms_read`, `mm`	1	1
	`ps`	3.673452	7.346903
	`nn`	0.001001	0.001001
	`qq`	1	1
	`taus`	1	1
Species 3	`ms_read`, `mm`	1836.1527	1836.1527
	`ps`	6.745018	13.490036
	`nn`	1.001001	1.001001
	`qq`	-1	-1
	`taus`	1	1

Table A.4: List of the resulting ALPS normalized parameters for a dense electron beam example.

A.3 ALPS input files

To write the input files for ALPS we will use the parameters listed in table A.4 as well as the ideal fit parameters obtained while generating the `f0-table`s. There is of course the possibility of generating the `f0-table`s in some other way, such as from observational data. In that case, it is recommended to fit the data beforehand and generate an initial guess for the fit parameters.

The ALPS input files allow for several types of scans which are described in the ALPS documentation. For analyzing the parallel propagating waves, it is best to do a $k_{||}$ scan (corresponding to scan type 4).

In order to find all the roots of the dispersion relation, it is useful to generate a map of the determinant of the dispersion tensor $\mathcal{D}$. This scan can allow us to find all of the roots of the dispersion relation by following each minimum found during the scan. However, one has to know where to look for the roots. An overview of space plasma instabilities can be found in Gary [1993].

A.4 Results

Just like the input files, the output files are normalized. We can use the electron skin depth d_p and the electron gyrofrequency Ω_e to convert the results to physical units.

For the example case introduced above, we present the dispersion relation for $v_b = 5w$ and $v_b = 10w$ as shown in figure A.1.

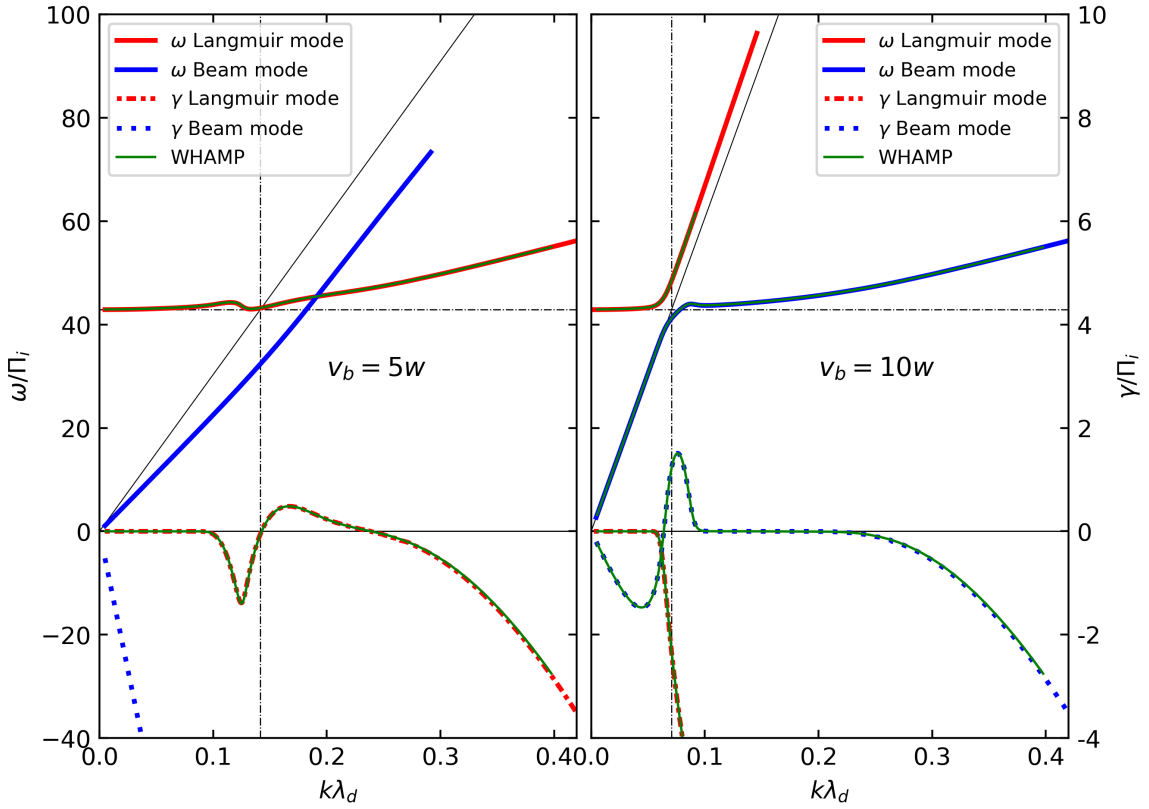

Figure A.1: The hot plasma dispersion relation calculated using the ALPS and WHAMP solvers. The dispersion relation roots corresponding to the Langmuir and beam modes are shown.

We also reproduced the results in the WHAMP dispersion relation solver. Both the frequency and growth rates coinside for both solvers as shown in figure A.1.